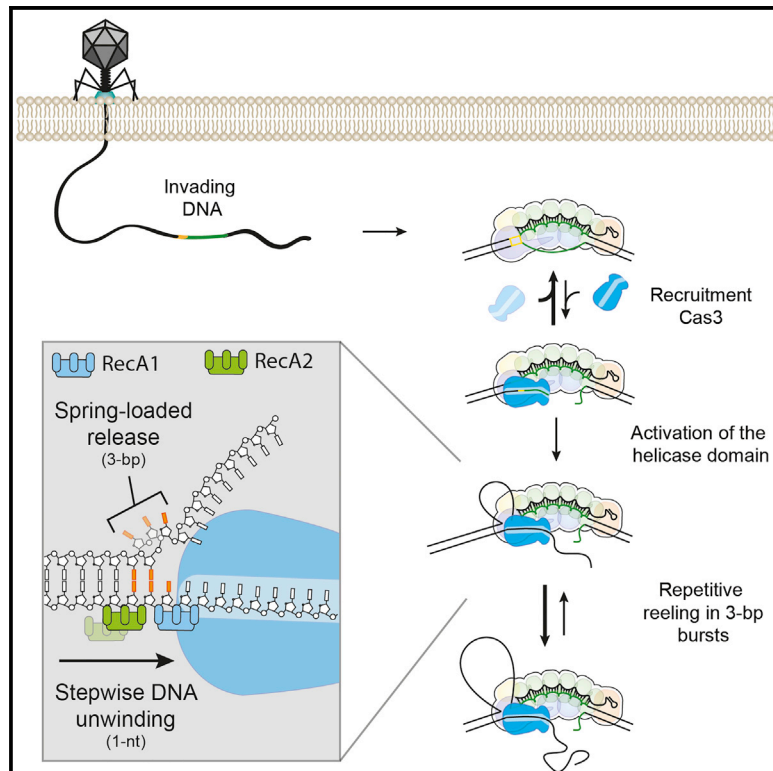


Repetitive DNA Reeling by the Cascade-Cas3 Complex in Nucleotide Unwinding Steps

Graphical Abstract



Authors

Luuk Loeff, Stan J.J. Brouns,
Chirlmin Joo

Correspondence

stanbrouns@gmail.com (S.J.J.B.),
c.joo@tudelft.nl (C.J.)

In Brief

Loeff et al. report on a single-molecule fluorescence analysis of the *E. coli* CRISPR-Cas3 protein. The Cas3 protein uses a spring-loaded unwinding mechanism, reeling the target DNA 3 bp at a time. Facilitated by slipping, Cas3 repeatedly presents its intrinsically inefficient nuclease domain with DNA substrate, which may contribute to promoting a robust immune response.

Highlights

- Cas3 reels target DNA in spring-loaded bursts 3 bp at a time
- The 3-bp bursts consist of a kinetic unwinding step size of 1 nt
- The nuclease domain of Cas3 is intrinsically inefficient in cleaving DNA
- The helicase domain repeatedly presents target DNA to the inefficient nuclease domain.



Repetitive DNA Reeling by the Cascade-Cas3 Complex in Nucleotide Unwinding Steps

Luuk Loeff,¹ Stan J.J. Brouns,^{1,2,*} and Chirlmin Joo^{1,3,*}¹Kavli Institute of Nanoscience and Department of Bionanoscience, Delft University of Technology, Delft 2629HZ, the Netherlands²Laboratory of Microbiology, Department of Agrotechnology and Food Sciences, Wageningen University, Wageningen 6708WE, the Netherlands³Lead Contact*Correspondence: stanbrouns@gmail.com (S.J.J.B.), c.joo@tudelft.nl (C.J.)<https://doi.org/10.1016/j.molcel.2018.03.031>

SUMMARY

CRISPR-Cas provides RNA-guided adaptive immunity against invading genetic elements. Interference in type I systems relies on the RNA-guided Cascade complex for target DNA recognition and the Cas3 helicase/nuclease protein for target degradation. Even though the biochemistry of CRISPR interference has been largely covered, the biophysics of DNA unwinding and coupling of the helicase and nuclease domains of Cas3 remains elusive. Here, we employed single-molecule Förster resonance energy transfer (FRET) to probe the helicase activity with high spatiotemporal resolution. We show that Cas3 remains tightly associated with the target-bound Cascade complex while reeling the DNA using a spring-loaded mechanism. This spring-loaded reeling occurs in distinct bursts of 3 bp, which underlie three successive 1-nt unwinding events. Reeling is highly repetitive, allowing Cas3 to repeatedly present its inefficient nuclease domain with single-strand DNA (ssDNA) substrate. Our study reveals that the discontinuous helicase properties of Cas3 and its tight interaction with Cascade ensure controlled degradation of target DNA only.

INTRODUCTION

Prokaryotes mediate defense against invading genetic elements using RNA-guided adaptive immune systems that are encoded by CRISPR (clustered regularly interspaced short palindromic repeats)-Cas (CRISPR-associated) loci (Barrangou et al., 2007; Marraffini and Sontheimer, 2008). In the type I system, the most ubiquitous CRISPR-Cas system (Makarova et al., 2015), foreign DNA targets (called protospacers) are recognized by the CRISPR RNA (crRNA)-guided surveillance complex Cascade (Brouns et al., 2008). Recognition of dsDNA targets results in the formation of an R-loop, in which the crRNA hybridizes with the complementary target strand and the non-complementary strand of the DNA is displaced (nontarget strand) (Blosser et al., 2015; Hayes et al., 2016; Jore et al., 2011; Mulepati et al., 2014; Rutkauskas et al.,

2015; Xiao et al., 2017). This R-loop formation triggers a conformational change in the Cascade complex (Blosser et al., 2015; Wiedenheft et al., 2011; Xiao et al., 2017; Xue et al., 2016) and leads to the recruitment of the Cas3 protein for subsequent target degradation (Hochstrasser et al., 2014; Sinkunas et al., 2011; Westra et al., 2012).

The *E. coli* Cas3 protein consists of two domains: a N-terminal metal-dependent histidine-aspartate (HD) nuclease domain and a C-terminal superfamily 2 helicase domain (Gong et al., 2014; Huo et al., 2014; Jackson et al., 2014; Makarova et al., 2015; Mulepati and Bailey, 2013; Sinkunas et al., 2011). Cas3 is activated by the Cascade-marked R-loop, where it cleaves the displaced nontarget strand ~11 nt into the R-loop region (Mulepati and Bailey, 2013; Sinkunas et al., 2013). Driven by ATP, Cas3 then moves along the nontarget strand in a 3' to 5' direction, while catalyzing cobalt-dependent DNA degradation (Mulepati and Bailey, 2013; Redding et al., 2015; Sinkunas et al., 2013; Westra et al., 2012). Subsequently, Cas3 generates degradation products that are close to spacer length and enriched for PAM-like NTT sequences in their 3' ends (Künne et al., 2016). This makes a considerable fraction of the degradation products suitable substrates for integration by the Cas1-Cas2 integrases into the CRISPR locus (Jackson et al., 2017; Künne et al., 2016). Even though the biochemistry of CRISPR interference has been largely covered, the biophysics of DNA unwinding by Cas3 remains elusive. In particular, how the helicase domain tunes the property of nuclease HD domain for spacer integration and how this process takes place in concert with Cascade.

RESULTS

Single-Molecule Observation of DNA Reeling by Cas3

We set out to understand how Cas3 unwinds double-stranded DNA (dsDNA) substrates. To date, two models prevail for DNA unwinding by the Cas3 helicase: a translocation model and a reeling model. In the translocation model, Cas3 breaks its contacts with the Cascade complex while unwinding the DNA. Thereby Cas3 translocates away from the Cascade binding site and degrades single-stranded DNA into fragments along the way (Figure 1A) (Hochstrasser et al., 2014; Mulepati and Bailey, 2013; Redding et al., 2015; Sinkunas et al., 2011; Staals et al., 2016; Westra et al., 2012). In the reeling model, Cas3 and Cascade remain in tight contact while Cas3 unwinds the DNA, which may result in loops in the target strand (Figure 1A)



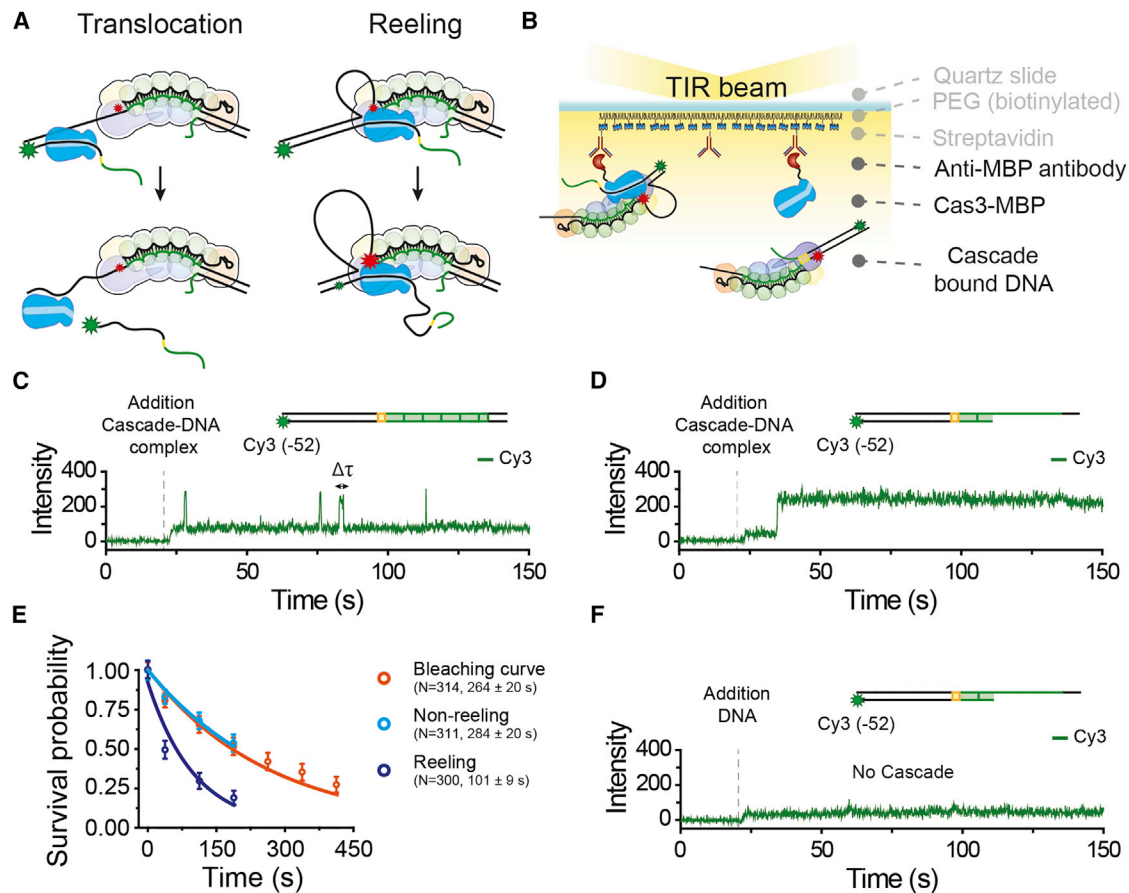


Figure 1. Single-Molecule Visualization of the Interaction between Cas3 and Cascade

(A) Schematic of two distinct models for DNA unwinding by Cas3. In the translocation model (left), Cas3 breaks its contacts with Cascade while it unwinds DNA. This results in translocation away from the Cascade target site. During DNA reeling (right), Cascade and Cas3 remain tightly associated while Cas3 pulls on the DNA. As a result, loops are formed in the target strand. The appearance of FRET during translocation or reeling is indicated by the size of the star: low FRET, large green star) or high FRET, large red star).

(B) Schematic of a single-molecule FRET assay used to probe the interaction between Cas3 and Cascade.

(C) A representative time trace of the initial interaction between Cas3 and Cascade bound to a cognate target labeled with a single fluorophore (Cy3).

(D) A representative time trace of the initial interaction between Cas3 and Cascade bound to a partial duplex target labeled with a single fluorophore (Cy3).

(E) Survival probability of fluorescence signals in absence of ATP (bleaching curve, orange circles), survival probability of the traces that displayed looping behavior (purple circles), and the molecules that did not show looping behavior (cyan circles). The lines represent a single-exponential fit. Error bars indicate the 95% confidence interval obtained by bootstrap analysis.

(F) A representative time trace of the initial interaction between Cas3 and a cognate target in absence of the Cascade complex.

See also Figure S1.

(Redding et al., 2015). To distinguish between these two models, we sought to visualize the DNA unwinding activity of Cas3 with a high spatiotemporal resolution.

To visualize DNA unwinding by Cas3, we developed an assay based on single-molecule Förster resonance energy transfer (smFRET). In brief, anti-maltose binding protein (MBP) antibodies were anchored to the surface of a polyethylene glycol (PEG)-coated slide through biotin-streptavidin linkage followed by tethering of MBP-fused Cas3 monomers (Figures 1B and S1A–S1C). Notably, the immobilization of Cas3 did not appreciably affect its capability to degrade dsDNA substrates (Figures S1C–S1G). Next, the antibody-tethered Cas3 molecules were presented to Cascade complexes bound to dye-labeled dsDNA substrates, and their interactions were probed in real time using

total internal reflection fluorescence (TIRF) microscopy (Figure 1B). We first explored the interaction of Cas3 with Cascade complexes that were bound to a fully complementary dsDNA target.

Introduction of the Cascade-DNA complexes in absence of cobalt resulted in a slight increase in the fluorescence background, followed by a sudden increase and subsequent rapid decrease in the fluorescence intensity. These transient interactions were observed with a dwell time ($\Delta\tau$) of 1.63 ± 0.236 s (Figures 1C and S1I) and reflect the initial interaction between the Cse1 subunit of the Cascade complex and the Cas3 protein (Brown et al., 2017; Hochstrasser et al., 2014; Huo et al., 2014). This finding is consistent with DNA curtain experiments where no stable interaction between Cascade and Cas3 was observed

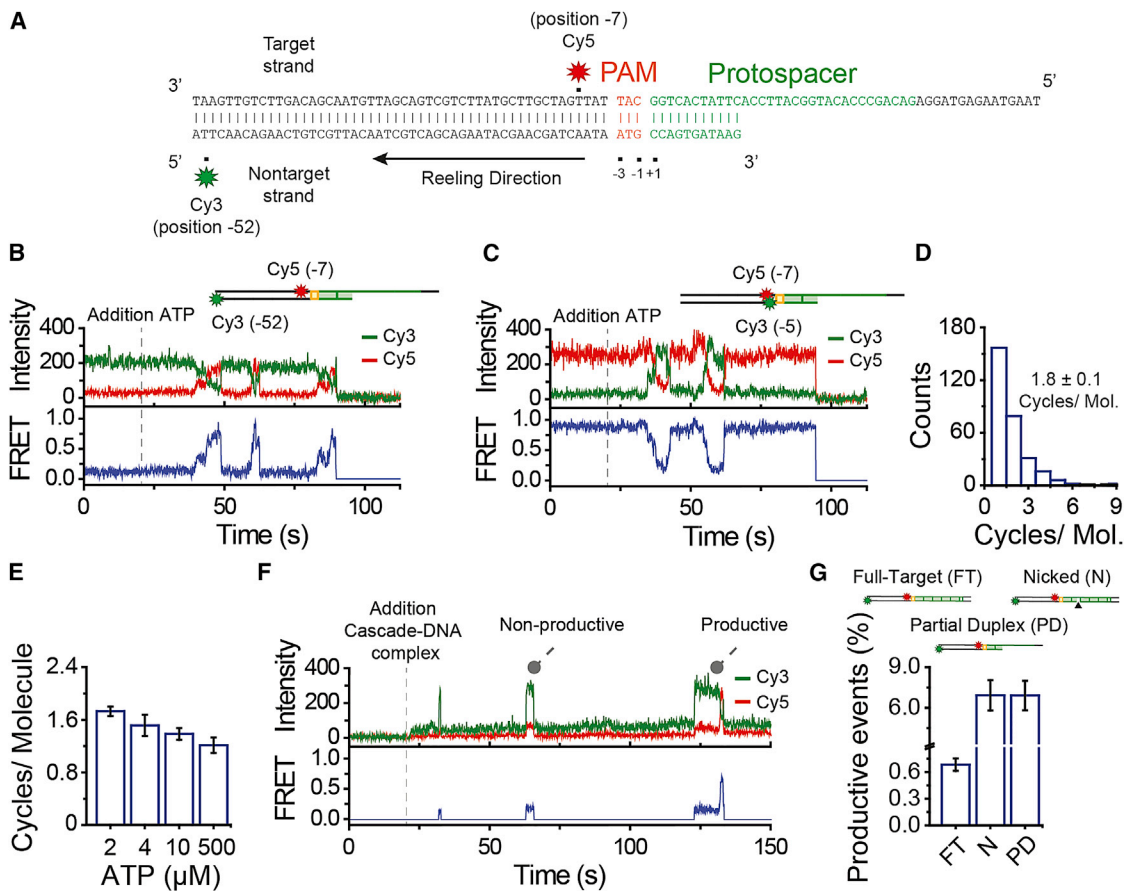


Figure 2. Real-Time Observation of DNA Reeling by Cas3

(A) Partial duplex DNA constructs consist of a PAM (orange), protospacer (green), and two flanks of 50 and 15 nt (black). Cy5 (red star) was attached to position -7 of the target strand and Cy3 (green star) to position -52 of the nontarget strand.

(B) A representative time trace of donor (Cy3, green) and acceptor (Cy5, red) fluorescence and corresponding FRET (blue) exhibiting multiple reeling events. ATP ($2 \mu\text{M}$) was added at $t = 20$ s (dashed gray line).

(C) A representative time trace for a construct with Cy5 (red star) attached to position -7 of the target strand and Cy3 (green star) to position -5 of the nontarget strand. ATP ($2 \mu\text{M}$) was added at $t = 20$ s (dashed gray line).

(D) A histogram representing the number of reeling cycles for each molecule. Error represents the SEM from three independent measurements ($n = 3$).

(E) Quantification of the number of reeling cycles per molecule at various ATP concentrations. Error bars represent the SEM ($n = 3$).

(F) Representative time traces of donor (Cy3, green) and acceptor (Cy5, red) fluorescence and corresponding FRET (blue) obtained by tracking the interactions by Cas3 and Cascade in real time. Cascade bound DNA, ATP ($500 \mu\text{M}$), and Co^{2+} ($10 \mu\text{M}$) were added at $t = 20$ s.

(G) Quantification of the number of productive binding events for three distinct DNA constructs. Cy5 (red star) was attached to position -7 of the target strand and Cy3 (green star) to position -52 of the nontarget strand. Black triangle indicates the position of the nick (11 nt away from PAM). Error bars represent the SEM ($n = 3$).

See also [Figures S2](#) and [S3](#).

when cobalt was omitted from the assay ([Brown et al., 2017](#); [Redding et al., 2015](#)). To focus on the Cas3 helicase activity, experiments were performed in the absence of cobalt, unless stated otherwise.

Next, the same experiment was repeated but with a partial dsDNA construct that mimicked the nicked R-loop reaction intermediate formed by Cas3 ([Figure 2A](#)). After equilibration, a stable interaction was observed for $69\% \pm 3\%$ of the molecules that showed interaction with the Cascade-DNA complex. This interaction lasted throughout the time course of the experiment and followed photo-bleaching kinetics ([Figures 1D](#) and [1E](#)). This suggests that the initial nick made by Cas3 facilitates loading of the

helicase domain, which stabilizes the interaction between Cas3 and the Cascade complex. Notably, the appearance of fluorescence signals was not observed when Cascade was omitted from the assay, confirming that Cas3 exclusively interacts with DNA in a Cascade-dependent manner ([Figures 1F](#) and [S1J](#)) ([Hayes et al., 2016](#); [Hochstrasser et al., 2014](#); [Jung et al., 2017](#); [Westra et al., 2012](#)).

To synchronize the initiation of DNA unwinding, experiments were continued with the partial dsDNA construct. The DNA substrate was labeled with a donor (Cy3) and an acceptor (Cy5) dye that were positioned such that it could report on reeling along the nontarget strand via an increase in FRET ([Figures 1A](#) and [2A](#);

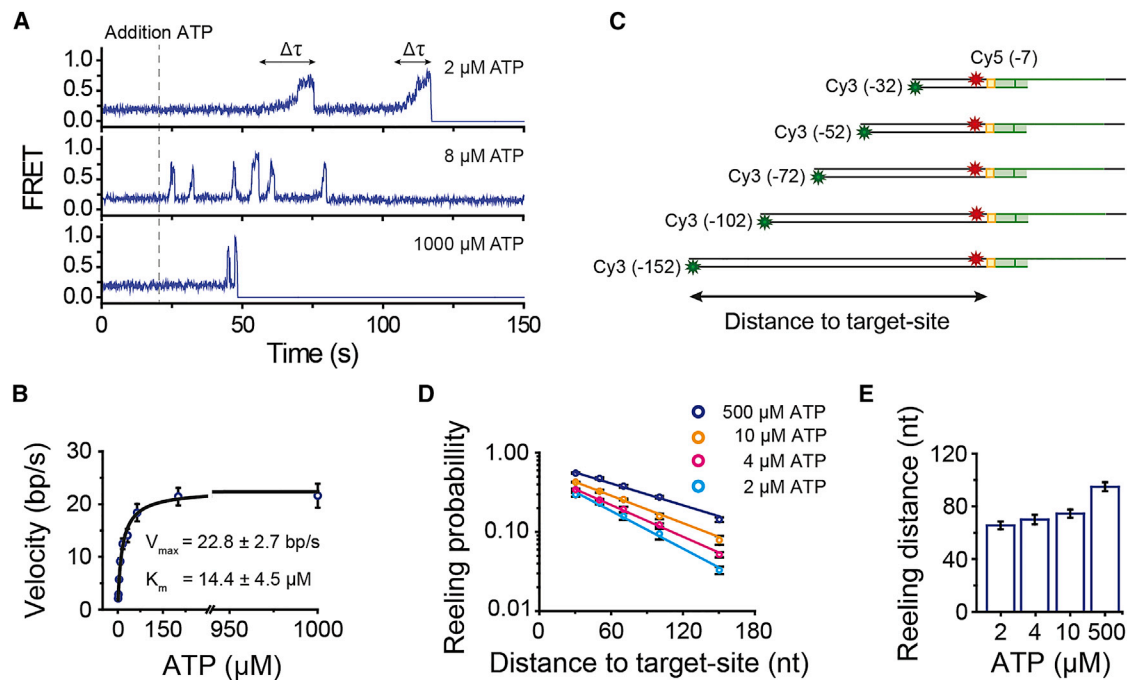


Figure 3. Velocity and Processivity of the Cas3 Helicase

(A) Representative FRET traces obtained at various ATP concentrations.

(B) Michaelis-Menten fit (black line) of the velocity (bp/s) plotted against the ATP concentration (1, 2, 4, 8, 16, 32, 64, 200, and 1,000 μM ATP). Error bars represent the 95% confidence interval obtained through bootstrap analysis.

(C) Schematic overview of constructs used to determine the mean reeling distance. Cy5 (red star) was attached to position -7 of the target strand and Cy3 (green star) was positioned at the end of the nontarget strand.

(D) Reeling probability over the distance to target site at various ATP concentrations. Error bars represent the SEM ($n = 3$). Solid lines represent a single-exponential fit used to determine the mean reeling distance.

(E) Bar plot with average reeling distance (nt) at various ATP concentrations. Error bars represent the SEM ($n = 3$).

See also Figure S4.

Table S1). The fluorescent probes were conjugated to the DNA using an amino-C6-linker, which has been shown not to interfere with the translocation and unwinding by helicases (Myong et al., 2005, 2007, 2009; Park et al., 2010). The target strand was labeled with Cy5 at nucleotide -7, which position is fixed near the Cascade complex (Hayes et al., 2016; Xiao et al., 2017), whereas the Cy3 dye was positioned further upstream of the PAM at position -52 of the nontarget strand (Figure 2A). In this configuration, a gradual increase in FRET would be observed upon reeling of the nontarget strand, whereas translocation would lead to a rapid loss of the donor signal (Figure 1A). In absence of ATP, no FRET was observed between the donor and acceptor fluorophore, resulting in FRET values that were indistinguishable from background signals ($E = 0.18$) (Figures 1B and S3A).

Upon introduction of ATP into the microfluidic chamber, a large fraction of the Cas3 molecules (201 out of 438 molecules) showed a gradual increase in FRET, which is consistent with reeling along the nontarget strand (Figures 2B and S2A). For remaining molecules, FRET stayed within background levels ($E = 0.18$). We hypothesize that these molecules either failed to initiate unwinding within our observation time (3.5 min) or did not reel the DNA beyond the FRET range of approximately 20 bp (Figure S5B). Consistent with the second hypothesis, the

probability of reeling scaled exponentially with the distance to the target site (Figure 3D). These data show that Cas3 remains anchored to Cascade while reeling the DNA. Notably, translocation of Cas3 away from the Cascade target site (Hochstrasser et al., 2014; Mulepati and Bailey, 2013; Redding et al., 2015; Sinkunas et al., 2011; Staals et al., 2016; Westra et al., 2012) would have been manifested by a rapid loss of the total fluorescence signal (Figure 1A), which was not observed under our tension free experimental conditions (Figure 1E). This is supported by the finding of tension dependent Cas3-Cascade rupture (Brown et al., 2017).

To confirm DNA reeling along the nontarget strand, we tested various alternative immobilization and labeling schemes. When the DNA (Figures S2C and S2D) or Cascade (Figures S2E and S2F) was immobilized or when the donor and acceptor dyes were swapped (Figures S3C and S3F), identical behavior was observed. Next, an alternative labeling scheme was tested, with a donor and acceptor dye at position -5 of the nontarget strand and -7 of the target strand, respectively. This construct initially yielded high FRET ($E = 0.8$, Figure S3B) and should lead to a decrease in FRET when reeling is triggered. In agreement with our expectation, FRET decreased upon introduction of ATP (Figures 2C and S2B). Notably, the proximity between the FRET pair in this configuration after the photophysics,

resulting in rapid photobleaching and limited statistics. DNA reeling along the nontarget strand was also observed using PIFE (protein-induced fluorescence enhancement) (Figure S2G). In contrast, when a construct was used that was designed to detect DNA reeling along the target strand (Cy3 position –52 target strand and Cy5 position –7 nontarget strand, Figure S3D) or when the PAM proximal and PAM distal flank were swapped (Figure S3E), a change in FRET was not observed (Figures S3G and S3H). These control experiments support the model that Cas3 remains anchored to Cascade when reeling in the 3' end of nontarget strand, resulting in DNA loops in the target strand.

Our real-time analysis of DNA reeling by Cas3 revealed that Cas3 could go through multiple cycles of reeling on a single substrate, by slipping back to its initial location (Figures 2B and 2C). Analysis of this repetitive behavior showed that Cas3 undergoes an average of 1.8 ± 0.1 cycles per substrate (Figure 2D). Interestingly, the number of reeling cycles per molecule decreased with an increase of ATP, reaching average unwinding frequency of 1.2 ± 0.1 cycles per molecule at saturating levels of ATP (Figure 2E). These data suggest that Cas3 is more effective in displacing the nontarget strand away from the Cas3-Cascade complex at higher levels of ATP, which is likely a result of using short DNA oligos. Consistent with this hypothesis, the dwell time of the looping population that reached the end of the substrate was ~ 3 times shorter as compared to the seemingly static population (Figure 1E).

Cas3 Exhibits Sparse Nuclease Activity

Next, we sought to determine how the repetitive reeling behavior is coordinated with the nuclease activity of the HD domain. Previous bulk experiments have shown that Cas3 degrades the nontarget strand while it moves along the DNA (Mulepati and Bailey, 2013; Sinkunas et al., 2013). Therefore, we hypothesized that activation of the nuclease domain, by the addition of Co^{2+} , would result in a stark decrease in the number of reeling cycles per molecule. However, no change in the number of cycles per molecule was observed when the nuclease domain was activated (Figure S3H), indicating that little nicking had occurred. Moreover, the addition of free Cas3 into the assay did not alter the behavior of Cas3 (data not shown). Consistent with this finding marginal degradation of the nontarget strand was observed in a biochemical assay on DNA oligos (Figure S1H).

To obtain a more quantitative estimate on the cleavage activity of Cas3, the initial interaction between Cas3 and Cascade was probed (Figure 2F). When Cascade bound to a full target substrate, without the initial nick, was introduced, only $0.7\% \pm 0.1\%$ of the binding events resulted in DNA reeling (Figures 2F and 2G). However, when Cascade was introduced bound to a substrate mimicking the nicked intermediate, the number of reeling events increased with an order of magnitude ($6.9\% \pm 1.1\%$, Figures 2F and 2G). This suggests that the HD nuclease domain intrinsically exhibits a sparse nuclease activity, which contrasts previously published bulk data (Hochstrasser et al., 2014; Künne et al., 2016; Mulepati and Bailey, 2013; Rollins et al., 2017; Sinkunas et al., 2013; Westra et al., 2012). Those bulk measurements were performed using a 10- to 500-fold excess of Cas3 (Hochstrasser et al., 2014; Künne et al., 2016; Mulepati and Bailey, 2013; Rollins et al., 2017; Sinkunas et al., 2013; Westra et al., 2012) that facilitated initial nicking and loading of the

Cas3 helicase, whereas here we used Cas3 in nanomolar concentrations. Our findings imply that the Cas3 protein compensates for the sparse nuclease activity by repeatedly reeling single-stranded DNA (ssDNA) substrates into the HD nuclease domain, which may ensure DNA cleavage.

Dynamics of DNA Loop Formation by Cas3

Next, we explored the molecular dynamics of DNA reeling by Cas3. To determine the unwinding rate of Cas3, we performed DNA unwinding assays at various ATP concentrations (Figures S4D–S4F). For every ATP concentration, the dwell time ($\Delta\tau$) of each unwinding event was extracted (Figure 3A), followed by fitting of the histograms with a gamma distribution (Figures S4A–S4C). Consistent with other helicases (Dumont et al., 2006; Myong et al., 2009; Park et al., 2010), the effective rate ($k_{\text{effective}}, 1/\Delta\tau$) increased with increasing amounts of ATP, indicating that the reeling velocity increases with ATP (Figure 3B). When ATP was replaced with a non-hydrolysable ATP analog ATP- γ -S, the reeling activity of Cas3 was completely abrogated (Figure S4G). To estimate the maximum velocity (V_{max}) of Cas3, the effective rate was converted to apparent velocity in base pairs per second (bp/s, see STAR Methods). By plotting the velocity over the ATP concentration and fitting the data with a Michaelis-Menten fit (Figure 3B), a $V_{\text{max}} = 22.8 \pm 2.7$ bp/s and $K_m = 14.4 \pm 4.5$ μM was obtained. Notably, only a marginal change in velocity was observed when the nuclease domain was activated (Figure S2I), suggesting that the reeling activity of the helicase domain dominates over the DNA degradation by the nuclease domain.

Recent DNA curtain experiments suggested that Cas3 is a highly processive molecular motor (Redding et al., 2015). However, given that the Cas3 nuclease exhibits sparse activity (Figures 2F and 2G), a highly processive motor would lead to single-stranded fragments that are much longer than the previously reported fragment size that is smaller than 200 nt (Künne et al., 2016; Mulepati and Bailey, 2013). Therefore, we sought to determine the average reeling distance of Cas3 at saturating concentrations of ATP. To estimate the reeling distance, a series of DNA substrates were used with an increasing length of the PAM proximal flank, while moving the donor dye toward the end of each substrate (Figure 3C). This set of constructs allowed for the determination of the probability that a Cas3 molecule reached the end of a DNA substrate within the observation time of 3.5 min.

Upon introduction of ATP, each construct yielded traces with identical behavior (Figures S4H–S4K). However, we observed a decrease in the number of events with an increase in the flank length, suggesting that the reeling probability decreased (Figure 3D). When the length of the flank was increased to 150 nt, the reeling probability decreased to 0.13 ± 0.1 (Figure 3D), suggesting that the majority of molecules formed loops smaller than 150 nt. To estimate the average unwinding distance, the reeling probability was plotted over the ATP concentration, followed by fitting each data series with a single-exponential decay. This yielded an average reeling distance of 95 ± 3 nt at a saturating ATP concentration (Figure 3E). A decrease in the average reeling distance was observed when the ATP concentration was lowered (Figure 3E). Notably, the addition of single stranded binding

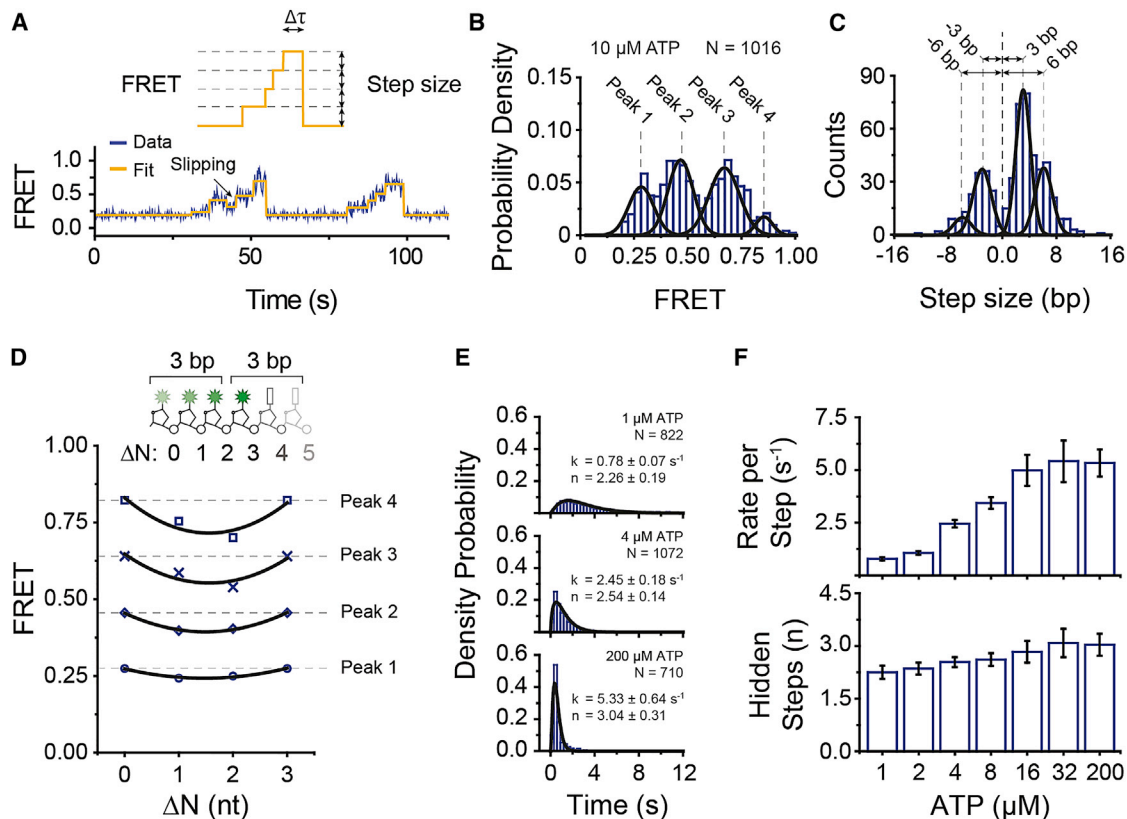


Figure 4. Cas3 Reels DNA in Uniform Steps

(A) Representative FRET trace (dark blue) fitted with a step-finder algorithm (orange).

(B) Distribution of FRET levels obtained through the step-finder algorithm. Black lines represent a Gaussian fit.

(C) Distribution of step sizes obtained through a step-finder algorithm. Black lines represent a Gaussian fit. Dashed gray lines indicate the center of each peak. Positive values represent processive reeling, whereas negative values represent slipping.

(D) Location of the FRET levels for various positions of the donor dye. Given the remarkable regularity in the reeling pattern of Cas3, we hypothesized that when moving the donor dye from its original position ($\Delta N = 0$) by 1 or 2 nt ($\Delta N = 1$ and $\Delta N = 2$, respectively) would shift the position of the observed plateaus at specific FRET levels. In contrast, moving the donor dyes by 3 nt ($\Delta N = 3$) locates the dye at a similar position as $\Delta N = 0$ (inset) and should yield identical FRET levels. Consistent with our hypothesis, the constructs with a donor dye at position $\Delta N = 1$ and $\Delta N = 2$ shifted the peak positions toward lower FRET values, whereas the construct with a dye at position $\Delta N = 3$ yielded identical FRET levels as $\Delta N = 0$ (Figure S5F).

(E) Dwell-time distributions of the FRET levels at various ATP concentrations. Data were fitted with a gamma distribution (solid line) to obtain the number of hidden steps (n) and rate (k). Error represents the 95% confidence interval obtained through bootstrap analysis.

(F) Bar plots representing the number of hidden steps (n) and rate (k) that was obtained through fitting dwell-time histograms with a gamma distribution. Error represents the 95% confidence interval obtained through bootstrap analysis.

See also Figure S5.

protein (SSB) did not alter the processivity of Cas3 (data not shown) (Brown et al., 2017), implying that Cas3 may shelter the looped target strand. These observations are in good agreement previously reported bulk biochemical data, which showed that Cas3 generates degradation products in the range of 30–150 nt that become smaller at low ATP concentrations (Dixon and Kowalczykowski, 1993; Künne et al., 2016; Mulepati and Bailey, 2013). Taken together, these results suggest that the helicase domain of Cas3 limits the fragment size by repeatedly generating a distribution ssDNA fragments with an average size of ~ 90 nt.

Cas3 Unwinds DNA in Uniform Steps

To understand what feature of the Cas3 helicase limits the reeling distance, we sought to understand the molecular mechanism

by which Cas3 unwinds the DNA. Close inspection of the FRET events revealed that FRET increased with a distinct pattern, marked by plateaus at specific FRET levels (Figure 4A). To elucidate this behavior, we employed an automated step-finder algorithm (Kerssemakers et al., 2006) (L.L., J. Kerssemakers, C.J., C. Dekker, unpublished data) that yielded the average FRET value for each plateau and the size of each step in between the plateaus (Figure 4A). Analysis of the average the FRET value for each plateau resulted in a histogram with four distinct peaks that were evenly separated ($\Delta E = 0.15$) (Figure 4B). To correlate these FRET values to distance in base pairs, we designed a series of DNA constructs, in which the distance between the dyes was systematically decreased (Figures S5A and S5B). The calibration experiment yielded a conversion factor, in which 1 bp

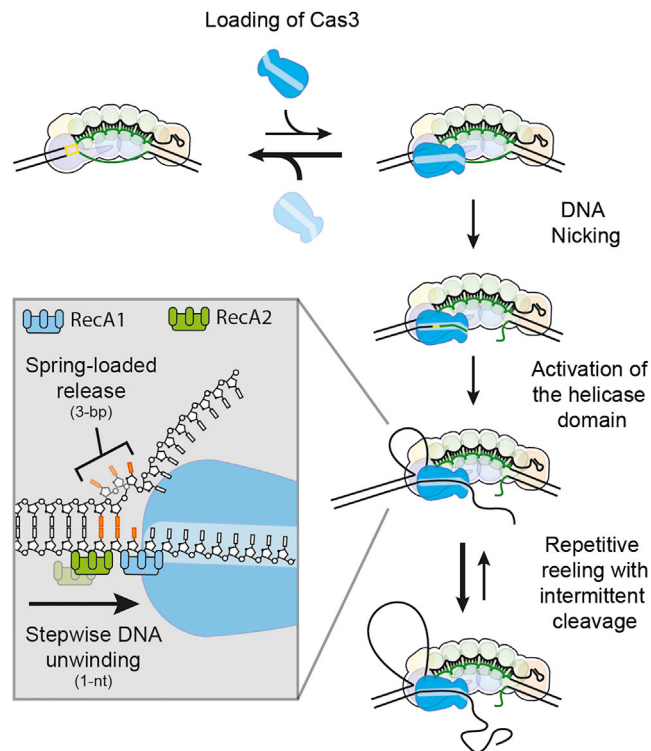


Figure 5. Model for CRISPR Interference-Mediated DNA Unwinding by Cas3

Model for CRISPR interference by Cas3. Interference starts with loading of the Cas3 protein onto the Cascade-DNA complex. Given the inherently sparse nuclease activity of Cas3, this may require multiple docking events. Once Cas3 nicks the R-loop, the loading of the helicase domain is facilitated, which allows Cas3 and Cascade to form a stable complex. Upon hydrolysis of ATP, Cas3 initiates DNA reeling that takes place in distinct spring-loaded steps of 3 bp and underlies an elementary step size of 1 nt. Cas3 repeatedly feeds ssDNA into its nuclease domain, which generates a distribution of degradation products with an average size of ~ 90 nt. See also [Videos S1](#) and [S2](#).

corresponds to a $\Delta E = 0.05$ FRET change. Notably, this conversion factor is in line with previously published work ([Blosser et al., 2009](#)). Conversion of the FRET values suggests that Cas3 reels the DNA with regular 3-bp steps.

To further characterize the stepping behavior of Cas3, a histogram was plotted with the distribution of step sizes, the distance between each plateau. The distribution of the step sizes exhibited a major peak centered at a step size of approximately 3 bp ([Figures 4C](#) and [S5B–S5D](#)), which is consistent with the histogram of average the FRET value for each plateau ([Figure 4B](#)). Apart from the major peak at 3 bp, minor peaks that represented a multiplicity of this step size (e.g., 6 bp) were observed ([Figures 4C](#) and [S5B–S5D](#)), which became more prominent when the ATP concentration was increased ([Figure S5D](#)). These larger steps are likely a result of a series of events that occur faster than our time resolution. Consistent with this hypothesis, a histogram of the average FRET levels at saturating concentration of ATP was skewed toward the high FRET states ([Figure S5E](#)). We confirmed the 3-bp step by designing a set of constructs in which the donor dye was shifted by 1, 2, or 3 nt ($\Delta N = 1$,

$\Delta N = 2$, and $\Delta N = 3$) from the standard construct ($\Delta N = 0$), resulting in 3-nt periodicity in FRET histograms ([Figure 4D](#)). These experiments provide strong evidence that Cas3 reels the DNA in distinct steps of 3 bp at a time.

Apart from steps that led to an increase in FRET, we also observed slipping events where the FRET signal abruptly dropped to intermediate levels ([Figure 4A](#)). These events were represented as a negative value in our step-size analysis and showed a major peak centered at -3 bp ([Figure 4C](#)). Besides the slipping events to intermediate levels, we also observed slipping events that returned to their initial FRET state ([Figures 2B](#) and [2C](#)). We speculate that these slipping events occur through miscoordination of the RecA-like domains of the Cas3 helicase ([Gong et al., 2014](#); [Huo et al., 2014](#)), leaving the DNA to zip back over a short or long distances. The short- and long-range slipping events result in discontinuous and burst-like unwinding behavior that allows Cas3 to repeatedly feed ssDNA fragments into the nuclease domain for further processing.

Finally, we questioned whether the observed 3-bp steps would correspond to the elementary step size of the Cas3 helicase. If Cas3 would unwind 3 bp upon the hydrolysis of a single ATP molecule, the dwell-time ($\Delta\tau$, [Figure 4A](#)) histogram of the FRET levels would follow a single-exponential decay. However, a dwell-time histogram of the FRET levels showed non-exponential behavior and followed a gamma distribution ([Figure 4E](#)). A fit of the histogram yielded a statistical description of the number of underlying hidden steps (n) and the rate per step (k) ([Figure 4E](#)). At various ATP concentrations, we obtained n values that remained close to three hidden steps, whereas the rate increased with an increase of ATP ([Figures 4E](#), [4F](#), and [S5H](#)). This analysis shows that each 3-bp step is composed of three hidden steps of 1 nt, suggesting that the elementary step size of Cas3 is 1 nt. From this analysis, the model emerges that Cas3 successively unwinds 3 bp in 1-nt steps, using its RecA-like domains ([Gong et al., 2014](#); [Huo et al., 2014](#)). During these successive 1-nt translocation events, the DNA is held in place by the Cas3 protein, resulting in an abrupt 3-bp spring-loaded burst upon release ([Video S1](#)).

DISCUSSION

Prokaryotes harbor CRISPR-Cas adaptive immune systems to eliminate invading phages and mobile genetic elements through CRISPR interference. In *E. coli*, CRISPR interference relies on the interplay of multiple proteins, providing robust resistance against foreign DNA. In this work, we leveraged the high spatial and temporal resolution of single-molecule FRET to obtain a mechanistic understanding on the molecular mechanisms that underlie tightly coordinated immune response. Based on our results, we propose a model in which the transacting Cas3 helicase/nuclease remains tightly anchored to the Cascade effector complex while repeatedly reeling the invader DNA in distinctive spring-loaded bursts of 3 bp ([Figure 5](#)).

Molecular Mechanism of Repetitive Reeling

Our single-molecule data reveal that Cas3 unwinds the DNA in 1-nt steps, presumably through successive movements of its RecA-like domains ([Figure 5](#); [Video S1](#)). While Cas3 opens the

dsDNA helix 1 nt at a time, the DNA is held in place until three of such steps have taken place (Figure 5; Video S1). This triggers the release of the DNA, resulting in a spring-loaded burst that moves the helicase by 3 bp. Such burst-like unwinding has been observed for other helicases with a RecA-like fold (such as NS3; Myong et al., 2007) and nucleases (Lee et al., 2011, 2012). Moreover, given that the helicase domain of Cas3 is highly conserved among different organisms (Jackson et al., 2014), this spring-loaded unwinding likely reflects a general feature of Cas3 proteins.

Our single-molecule data show that once Cas3 is loaded onto the Cascade complex, Cas3 goes through multiple cycles of reeling on the same DNA substrate. This unwinding behavior allows Cas3 to repeatedly present its nuclease domain with ssDNA substrate. We speculate that this repetitive behavior provides a means to compensate for the sparse activity of the nuclease domain. Additionally, repetitive unwinding allows Cas3 to repeatedly probe the DNA for thymine-rich sequences, which are preferred cleavage sites for the Cas3 nuclease (Künne et al., 2016).

Reeling in the Context of Primed Spacer Acquisition

To cope with mutated invaders, the CRISPR immune system employs a mechanism, called primed spacer acquisition, that facilitates rapid acquisition of new spacers to restore the immunological memory (Datsenko et al., 2012; Fineran et al., 2014). Recent studies have shown that degradation products of CRISPR interference can be repurposed as spacer precursors, which fuels primed spacer acquisition (Künne et al., 2016; Staals et al., 2016; Swarts et al., 2012). This coupling of CRISPR interference and primed spacer acquisition allows the host to keep pace with the escape strategies of the phage, such as genetic mutations and anti-CRISPR proteins (Staals et al., 2016).

Our data reveal that the intrinsic properties of the helicase domain facilitate slipping, which limits its unwinding distance. This repetitive reeling provides a mechanism for the helicase domain to repeatedly feed sized fragments into the nuclease domain. This mechanism could allow Cas3 to generate precursors for the Cas1-Cas2 integrase complex that are close to spacer size and enriched for NTT in their 3' ends (Figure 5) (Künne et al., 2016). Interestingly, our data show that, when the helicase is provided with low amounts of ATP, the average translocation distance of Cas3 remains approximately twice the size of a mature protospacer (Figure 3E). This suggests that the Cas3 helicase is tuned to allow the generation of pre-spacers for integration over a broad spectrum of intracellular ATP levels, providing an additional layer of robustness to the immune system.

Apart from the RecA-like domains, the Cas3 helicase is equipped with an accessory C-terminal domain (CTD), which packs on top of both RecA domains (Gong et al., 2014; Huo et al., 2014). *In vitro* experiments have shown that deletion of the CTD of Cas3 (Δ CTD) weakens the affinity of Cas3 for Cascade and reduces CRISPR interference to helicase null mutant levels (Huo et al., 2014). The CTD of Cas3 has therefore been suggested to play a role in loading of the helicase domain. In related helicases with a similar configuration of the CTD, the CTD often functions as a backstop, facilitating directional unwinding (Fairman-Williams et al., 2010; Jackson et al., 2014; Myong et al., 2007). Based on these findings, we speculate that the CTD of

Cas3 is responsible for holding the unwound nucleotides. The CTD may additionally attenuate the slipping distance, as our data show that the majority of slipping events by the Cas3 helicase is limited to a distance of 3 bp (Video S2). The fine balance between short range (3 bp) and long range (>20 bp) allows Cas3 to repeatedly unwind the DNA over a defined length. This behavior contrasts other SF2 helicases where slipping occurs in a less controlled manner, resulting in slipping events that return the helicase to its initiation site. A mutational study combined with deep sequencing could further reveal the role of CTD of Cas3 in light of spacer acquisition.

STAR★METHODS

Detailed methods are provided in the online version of this paper and include the following:

- KEY RESOURCES TABLE
- CONTACT FOR REAGENT AND RESOURCE SHARING
- METHOD DETAILS
 - Protein preparation
 - Cas3 degradation Assays
 - DNA preparation
 - Single-molecule fluorescence data acquisition
 - Single-molecule fluorescence data analysis
- QUANTIFICATION AND STATISTICAL ANALYSIS

SUPPLEMENTAL INFORMATION

Supplemental Information includes five figures, one table, and two videos and can be found with this article online at <https://doi.org/10.1016/j.molcel.2018.03.031>.

ACKNOWLEDGMENTS

C.J. was funded by the Open Program of the Division for Earth and Life Sciences (822.02.008) and Vidi (864.14.002) of the Netherlands Organization for Scientific research. S.J.J.B. was funded by an LS6 ERC starting grant (639707) and a NWO VIDI grant (864.11.005). We would like to thank S. Bailey (Johns Hopkins University) for providing the Cas3 overexpression construct. We thank T. Blosser, T. Künne, M. Klein, and R. McKenzie for critically reading this manuscript, and we thank A.C. Haagsma, M. Klein, M. Depken, M. Szczepaniak, and J. Kerssemakers for technical support.

AUTHOR CONTRIBUTIONS

L.L., S.J.J.B., and C.J. conceived the study; L.L. performed experiments; L.L. analyzed data; L.L., S.J.J.B., and C.J. discussed the data and wrote the paper.

DECLARATION OF INTERESTS

The authors declare no competing interests.

Received: November 24, 2017

Revised: February 23, 2018

Accepted: March 24, 2018

Published: April 26, 2018

REFERENCES

Barrangou, R., Fremaux, C., Deveau, H., Richards, M., Boyaval, P., Moineau, S., Romero, D., and Horvath, P. (2007). CRISPR provides acquired resistance against viruses in prokaryotes. *Science* 315, 1709–1712.

- Blosser, T.R., Yang, J.G., Stone, M.D., Narlikar, G.J., and Zhuang, X. (2009). Dynamics of nucleosome remodelling by individual ACF complexes. *Nature* 462, 1022–1027.
- Blosser, T.R., Loeff, L., Westra, E.R., Vlot, M., Künne, T., Sobota, M., Dekker, C., Brouns, S.J.J., and Joo, C. (2015). Two distinct DNA binding modes guide dual roles of a CRISPR-Cas protein complex. *Mol. Cell* 58, 60–70.
- Brouns, S.J.J., Jore, M.M., Lundgren, M., Westra, E.R., Slijkuis, R.J.H., Snijders, A.P.L., Dickman, M.J., Makarova, K.S., Koonin, E.V., and van der Oost, J. (2008). Small CRISPR RNAs guide antiviral defense in prokaryotes. *Science* 321, 960–964.
- Brown, M.W., Dillard, K.E., Xiao, Y., Dolan, A., Hernandez, E., Dahlhauser, S., Kim, Y., Myler, L.R., Anslyn, E., Ke, A., et al. (2017). Assembly and translocation of a CRISPR-Cas primed acquisition complex. *bioRxiv* <https://doi.org/10.1101/208058>.
- Chandradoss, S.D., Haagsma, A.C., Lee, Y.K., Hwang, J.-H., Nam, J.-M., and Joo, C. (2014). Surface passivation for single-molecule protein studies. *J. Vis. Exp.* Published online April 24, 2014. <https://doi.org/10.3791/50549>.
- Datsenko, K.A., Pougach, K., Tikhonov, A., Wanner, B.L., Severinov, K., and Semenov, E. (2012). Molecular memory of prior infections activates the CRISPR/Cas adaptive bacterial immunity system. *Nat. Commun.* 3, 945.
- Dekking, F.M. (2005). *A Modern Introduction to Probability and Statistics: Understanding why and how* (Springer Science & Business Media).
- Dixon, D.A., and Kowalczykowski, S.C. (1993). The recombination hotspot chi is a regulatory sequence that acts by attenuating the nuclease activity of the *E. coli* RecBCD enzyme. *Cell* 73, 87–96.
- Dumont, S., Cheng, W., Serebrov, V., Beran, R.K., Tinoco, I., Jr., Pyle, A.M., and Bustamante, C. (2006). RNA translocation and unwinding mechanism of HCV NS3 helicase and its coordination by ATP. *Nature* 439, 105–108.
- Fairman-Williams, M.E., Guenther, U.P., and Jankowsky, E. (2010). SF1 and SF2 helicases: Family matters. *Curr. Opin. Struct. Biol.* 20, 313–324.
- Fineran, P.C., Gerritsen, M.J.H., Suárez-Diez, M., Künne, T., Boekhorst, J., van Hijum, S.A.F.T., Staals, R.H.J., and Brouns, S.J.J. (2014). Degenerate target sites mediate rapid primed CRISPR adaptation. *Proc. Natl. Acad. Sci. USA* 111, E1629–E1638.
- Gong, B., Shin, M., Sun, J., Jung, C.-H., Bolt, E.L., van der Oost, J., and Kim, J.-S. (2014). Molecular insights into DNA interference by CRISPR-associated nuclease-helicase Cas3. *Proc. Natl. Acad. Sci. USA* 111, 16359–16364.
- Hayes, R.P., Xiao, Y., Ding, F., van Erp, P.B.G., Rajashankar, K., Bailey, S., Wiedenheft, B., and Ke, A. (2016). Structural basis for promiscuous PAM recognition in type I-E Cascade from *E. coli*. *Nature* 530, 499–503.
- Hochstrasser, M.L., Taylor, D.W., Bhat, P., Guegler, C.K., Sternberg, S.H., Nogales, E., and Doudna, J.A. (2014). CasA mediates Cas3-catalyzed target degradation during CRISPR RNA-guided interference. *Proc. Natl. Acad. Sci. USA* 111, 6618–6623.
- Huo, Y., Nam, K.H., Ding, F., Lee, H., Wu, L., Xiao, Y., Farchione, M.D., Jr., Zhou, S., Rajashankar, K., Kurinov, I., et al. (2014). Structures of CRISPR Cas3 offer mechanistic insights into Cascade-activated DNA unwinding and degradation. *Nat. Struct. Mol. Biol.* 21, 771–777.
- Jackson, R.N., Lavin, M., Carter, J., and Wiedenheft, B. (2014). Fitting CRISPR-associated Cas3 into the helicase family tree. *Curr. Opin. Struct. Biol.* 24, 106–114.
- Jackson, S.A., McKenzie, R.E., Fagerlund, R.D., Kieper, S.N., Fineran, P.C., and Brouns, S.J.J. (2017). CRISPR-Cas: Adapting to change. *Science* 356, 1–9.
- Jore, M.M., Lundgren, M., van Duijn, E., Bultema, J.B., Westra, E.R., Waghmare, S.P., Wiedenheft, B., Pul, U., Wurm, R., Wagner, R., et al. (2011). Structural basis for CRISPR RNA-guided DNA recognition by Cascade. *Nat. Struct. Mol. Biol.* 18, 529–536.
- Jung, C., Hawkins, J.A., Jones, S.K., Jr., Xiao, Y., Rybarski, J.R., Dillard, K.E., Hussmann, J., Saifuddin, F.A., Savran, C.A., Ellington, A.D., et al. (2017). Massively parallel biophysical analysis of CRISPR-Cas complexes on next generation sequencing chips. *Cell* 170, 35–47.
- Kerssemakers, J.W.J., Munteanu, E.L., Laan, L., Noetzel, T.L., Janson, M.E., and Dogterom, M. (2006). Assembly dynamics of microtubules at molecular resolution. *Nature* 442, 709–712.
- Künne, T., Kieper, S.N., Bannenberg, J.W., Vogel, A.I.M., Mielliet, W.R., Klein, M., Depken, M., Suarez-Diez, M., and Brouns, S.J.J. (2016). Cas3-derived target DNA degradation fragments fuel primed CRISPR adaptation. *Mol. Cell* 63, 852–864.
- Lee, G., Yoo, J., Leslie, B.J., and Ha, T. (2011). Single-molecule analysis reveals three phases of DNA degradation by an exonuclease. *Nat. Chem. Biol.* 7, 367–374.
- Lee, G., Bratkowski, M.A., Ding, F., Ke, A., and Ha, T. (2012). Elastic coupling between RNA degradation and unwinding by an exonuclease. *Science* 336, 1726–1729.
- Makarova, K.S., Wolf, Y.I., Alkhnbashi, O.S., Costa, F., Shah, S.A., Saunders, S.J., Barrangou, R., Brouns, S.J.J., Charpentier, E., Haft, D.H., et al. (2015). An updated evolutionary classification of CRISPR-Cas systems. *Nat. Rev. Microbiol.* 13, 722–736.
- Marraffini, L.A., and Sontheimer, E.J. (2008). CRISPR interference limits horizontal gene transfer in staphylococci by targeting DNA. *Science* 322, 1843–1845.
- Mulepati, S., and Bailey, S. (2013). In vitro reconstitution of an *Escherichia coli* RNA-guided immune system reveals unidirectional, ATP-dependent degradation of DNA target. *J. Biol. Chem.* 288, 22184–22192.
- Mulepati, S., Héroux, A., and Bailey, S. (2014). Structural biology. Crystal structure of a CRISPR RNA-guided surveillance complex bound to a ssDNA target. *Science* 345, 1479–1484.
- Myong, S., Rasnik, I., Joo, C., Lohman, T.M., and Ha, T. (2005). Repetitive shuttling of a motor protein on DNA. *Nature* 437, 1321–1325.
- Myong, S., Bruno, M.M., Pyle, A.M., and Ha, T. (2007). Spring-loaded mechanism of DNA unwinding by hepatitis C virus NS3 helicase. *Science* 317, 513–516.
- Myong, S., Cui, S., Cornish, P.V., Kirchhofer, A., Gack, M.U., Jung, J.U., Hopfner, K.P., and Ha, T. (2009). Cytosolic viral sensor RIG-I is a 5'-triphosphate-dependent translocase on double-stranded RNA. *Science* 323, 1070–1074.
- Pan, H., Xia, Y., Qin, M., Cao, Y., and Wang, W. (2015). A simple procedure to improve the surface passivation for single molecule fluorescence studies. *Phys. Biol.* 12, 045006.
- Park, J., Myong, S., Niedziela-Majka, A., Lee, K.S., Yu, J., Lohman, T.M., and Ha, T. (2010). PcrA helicase dismantles RecA filaments by reeling in DNA in uniform steps. *Cell* 142, 544–555.
- Redding, S., Sternberg, S.H., Marshall, M., Gibb, B., Bhat, P., Guegler, C.K., Wiedenheft, B., Doudna, J.A., and Greene, E.C. (2015). Surveillance and Processing of Foreign DNA by the *Escherichia coli* CRISPR-Cas System. *Cell* 163, 854–865.
- Rollins, M.F., Chowdhury, S., Carter, J., Golden, S.M., Wilkinson, R.A., Bondy-Denomy, J., Lander, G.C., and Wiedenheft, B. (2017). Cas1 and the Csy complex are opposing regulators of Cas2/3 nuclease activity. *Proc. Natl. Acad. Sci. USA* 114, E5113–E5121.
- Rutkauskas, M., Sinkunas, T., Songailiene, I., Tikhomirova, M.S., Siksnys, V., and Seidel, R. (2015). Directional R-loop formation by the CRISPR-cas surveillance complex cascade provides efficient off-target site rejection. *Cell Rep.* 10, 1534–1543.
- Sinkunas, T., Gasiunas, G., Fremaux, C., Barrangou, R., Horvath, P., and Siksnys, V. (2011). Cas3 is a single-stranded DNA nuclease and ATP-dependent helicase in the CRISPR/Cas immune system. *EMBO J.* 30, 1335–1342.
- Sinkunas, T., Gasiunas, G., Waghmare, S.P., Dickman, M.J., Barrangou, R., Horvath, P., and Siksnys, V. (2013). In vitro reconstitution of Cascade-mediated CRISPR immunity in *Streptococcus thermophilus*. *EMBO J.* 32, 385–394.

- Staals, R.H.J., Jackson, S.A., Biswas, A., Brouns, S.J.J., Brown, C.M., and Fineran, P.C. (2016). Interference dominates and amplifies spacer acquisition in a native CRISPR-Cas system. *Nat. Commun.* 23, 127–135.
- Swarts, D.C., Mosterd, C., van Passel, M.W.J., and Brouns, S.J.J. (2012). CRISPR interference directs strand specific spacer acquisition. *PLoS ONE*. Published online April 27, 2012. <https://doi.org/10.1371/journal.pone.0035888>.
- Westra, E.R., van Erp, P.B.G., Künne, T., Wong, S.P., Staals, R.H.J., Seegers, C.L.C., Bollen, S., Jore, M.M., Semenova, E., Severinov, K., et al. (2012). CRISPR immunity relies on the consecutive binding and degradation of negatively supercoiled invader DNA by Cascade and Cas3. *Mol. Cell* 46, 595–605.
- Wiedenheft, B., Lander, G.C., Zhou, K., Jore, M.M., Brouns, S.J.J., van der Oost, J., Doudna, J.A., and Nogales, E. (2011). Structures of the RNA-guided surveillance complex from a bacterial immune system. *Nature* 477, 486–489.
- Xiao, Y., Luo, M., Hayes, R.P., Kim, J., Ng, S., Ding, F., Liao, M., Ke, A., Ding, F., Liao, M., et al. (2017). Structure basis for directional R-loop formation and substrate handover mechanisms in type I CRISPR-Cas system. *Cell* 170, 48–60.
- Xue, C., Whittis, N.R., Sashital, D.G., Xue, C., Whittis, N.R., and Sashital, D.G. (2016). Conformational control of cascade interference and priming activities in CRISPR immunity. *Mol. Cell* 64, 1–9.

STAR★METHODS

KEY RESOURCES TABLE

REAGENT or RESOURCE	SOURCE	IDENTIFIER
Antibodies		
Anti-MBP antibody (Goat)	US Biological Life Sciences	Cat# M2155-09P
Bacterial and Virus Strains		
BL21-AI competent cell	Thermo Fisher Scientific	Cat# C607003
BL21-DE3	Jore et al., 2011 ; NSMB	N/A
Chemicals, Peptides, and Recombinant Proteins		
NHS-Cy3	GE Healthcare	Cat# PA13101
NHS-Cy5	GE Healthcare	Cat# PA15101
ATP	Sigma	Cat# A6559-25UMO
ATP- γ -s	Sigma	Cat# 808539
mPEG (MW 5,000)	Lysan	Cat# MPEG-SVA-5000-1g
mPEG-biotin (MW 5,000)	Lysan	Cat# Biotin-PEG-SVA-100mg
Amino-silane	Sigma	Cat# 281778
MS4-PEG	Thermo Fisher Scientific	Cat# 22341
Streptavidin	Invitrogen	Cat# S-888
Glucose oxidase	Sigma	Cat# G2133
TROLOX	Sigma	Cat# 238813
Catalase	Roche	Cat# 10106810001
HEPES	Sigma	Cat# H3375
KCl	Ambion	Cat# AM9530G
MgCl ₂	Ambion	Cat# AM9640G
CoCl ₂	Sigma	Cat# 1001695330
NiCl ₂	Sigma	Cat# 1001704316
EDTA	Ambion	Cat# AM9261
Proteinase K	Sigma	Cat# P6556
Oligonucleotides		
See Table S1	This study	N/A
Recombinant DNA		
M13mp18	New England Biolabs	Cat# N4040S
pCDF1-1b (Cse2, Ca, Cas6, Cas7)	Jore et al., 2011	N/A
pRSF-1b (Cse1)	Jore et al., 2011	N/A
pACYCduet (crRNA)	Jore et al., 2011	N/A
pMAT (Cas3-MBP)	Mulepati and Bailey, 2013	N/A
Software and Algorithms		
Stepfinder (MATLAB, Mathworks)	Kerssemakers et al., 2006	N/A
MATLAB (Mathworks)	https://www.mathworks.com	N/A
IDL (ITT visual information solutions)	http://www.harrisgeospatial.com/	N/A

CONTACT FOR REAGENT AND RESOURCE SHARING

As Lead Contact, Chirlmin Joo is responsible for all reagent and resource requests. Please contact Chirlmin Joo at c.joo@tudelft.nl with requests and inquiries.

METHOD DETAILS

Protein preparation

Cascade was expressed in *E. coli* BL21 (DE3) and purified using strep-tag affinity chromatography (Jore et al., 2011). Purified Cascade complexes were aliquoted and flash frozen in liquid nitrogen for long-term storage at -80°C . The MBP tagged nuclease-helicase Cas3 was expressed in *E. coli* BL21 (AI) by induction with 0.5 mM IPTG and 0.2% L-Arabinose. Cas3-MBP was purified using 6xhis-tag affinity chromatography, followed by size exclusion chromatography (Superdex 200 increase 10/300 GL) (Mulepati and Bailey, 2013). The purification process was stopped after size exclusion chromatography and before the proteolytic removal of the Maltose Binding Protein (MBP) using the Tobacco Edge Virus protease (Hochstrasser et al., 2014). MBP-Cas3 was aliquoted and flash frozen in liquid nitrogen before storage at -80°C .

Cas3 degradation Assays

After purification, Cas3 nuclease activity was initially tested by a non-specific degradation assay. In brief, 4 nM M13mp8 single-stranded circular DNA was incubated with 500 nM Cas3 and 150 μM Ni^{+2} ions in buffer R (50 mM HEPES (pH 7.5), 60 mM KCl, 10 mM MgCl_2) for 1 hour at 37°C (Figure S1B) (Mulepati and Bailey, 2013). After incubation, samples were quenched with TriTrack DNA loading Dye (R1161, Thermo fisher) and ran on a 1.5% agarose gel for 1 hour at 120V. Gels were imaged using GelDoc XR (Biorad).

To test specific degradation plasmid-based assays were performed in the presence of Cascade, ATP, Mg^{+2} and Co^{+2} ions (Figures S1C–S1E) (Künne et al., 2016; Mulepati and Bailey, 2013). Similar conditions were used for oligo based degradation assays (Figure S1H). In brief, for both plasmid and oligo degradation assays, 5 nM DNA was incubated with 50 nM Cascade and 100 nM Cas3 in buffer R (supplemented with 10 μM CoCl_2 and 2 mM ATP) for 30 minutes at 37°C . Samples were immediately quenched by adding stop solution (20 mM Tris-HCl pH 8.0, 2% SDS, 50 mM EDTA), after which protein was removed by incubating the samples for 1 hour with 10 $\mu\text{g}/\text{ml}$ proteinase K (Sigma) at 50°C . Subsequently, DNA was precipitated with ethanol and loaded on 10% denaturing PAGE gels (8M urea) with formamide. Gels were run for 2.5 hour at 350 V, followed by imaging with the Typhoon trio (GE healthcare).

DNA preparation

All the target dsDNA substrates that we used were bearing a protospacer, PAM, and two flanks of 50 and 15 nt (Figure 2A; Table S1). These synthetic DNA targets (Ella Biotech GmbH) were internally labeled with a monoreactive acceptor dye (Cy5, GE Healthcare) at dT-C6 on the target strand (complementary to the crRNA) and a monoreactive donor dye (Cy3, GE Healthcare) at dT-C6 on the nontarget strand (Figure 2A). After labeling, the ssDNA strands were annealed using a thermocycler (Biorad). To determine the initial FRET values of these constructs (Figures S3A–S3E and S5B), Cascade bound DNA was docked on the surface immobilized Cas3 molecules in absence of ATP.

Single-molecule fluorescence data acquisition

The fluorescent label Cy3 and Cy5 were imaged using prism-type total internal reflection microscopy (Blosser et al., 2015). In brief, the fluorescent label Cy3 was imaged through excitation by a 532nm (Compass 215M-50, Coherent). Cy5 was detected via FRET with Cy3, but if necessary, Cy5 was directly excited using a 640nm solid-state laser (CUBE 640-100C, Coherent). Fluorescence signals from single molecules were collected through a 60x water immersion objective (UPlanSApo, Olympus) with an inverted microscope (IX71, Olympus). Scattering of the 532nm laser beam was blocked with a 550nm long-pass filter (LP03-532RU-25, SemRock). When the 640nm laser was used, 640nm laser scattering was blocked with a notch filter ($633 \pm 12.5\text{nm}$, NF03-633E-25, SemRock). Subsequently, signals of Cy3 and Cy5 were spectrally split with a dichroic mirror ($\lambda^{\text{cutoff}} = 645\text{nm}$, Chroma) and imaged onto to halves of an electron multiplying CCD camera (iXon 897, Andor Technology).

To eliminate non-specific surface adsorption of proteins and nucleic acids to a quartz surface (Finkenbeiner), piranha-etched slides were PEG-passivated over two rounds of PEGylation (Chandradoss et al., 2014). After assembly of a microfluidic flow chamber, slides were incubated for 10 minutes with 5% Tween20 to further improve slide quality (Pan et al., 2015). Next, the chamber was incubated with 20 μL streptavidin (0.1 mg/ml, S-888, Invitrogen) for 5 minutes followed by a washing step with 100 μL of buffer R. Anti-Maltose Binding Protein (anti-MBP) antibodies (M2155-09P, US biological life sciences) were specifically immobilized through biotin-streptavidin linkage by incubating the chamber with 40 μL of 10 $\mu\text{g}/\text{ml}$ anti-MBP antibodies for 5 minutes. Remaining unbound anti-MBP antibodies were flushed away with 100 μL buffer R. Subsequently, 100 μL of 10 nM Cas3-MBP was incubated in the chamber, allowing the Cas3-MBP molecules to bind the surface immobilized anti-MBP antibodies. After 5 minutes of incubation, unbound Cas3-MBP molecules were flushed away with 100 μL buffer R^{imaging} (50 mM HEPES (pH 7.5), 60 mM KCl, 10 mM MgCl_2 , 0.1 mg/ml glucose oxidase (G2133, Sigma), 4 $\mu\text{g}/\text{ml}$ Catalase (10106810001, Roche) and 1 mM Trolox (((\pm)-6-Hydroxy-2,5,7,8-tetramethylchromane-2-carboxylic acid, 238813, Sigma).

Cascade was incubated with 5 nM labeled dsDNA substrate with 50 nM Cascade for 5 minutes at 37°C . For docking experiments, pre-bound Cascade-DNA complexes were introduced in the chamber with 500 μM ATP and 10 μM Co^{2+} while imaging at room temperature ($23 \pm 1^{\circ}\text{C}$) and binding events were monitored in real time. For DNA unwinding assays the Cascade-DNA complexes were incubated for 5 minutes, allowing the complexes to form a stable interaction with the surface immobilized Cas3 molecules. Reeling was initiated by introducing ATP into the chamber while imaging at room temperature ($23 \pm 1^{\circ}\text{C}$), allowing for visualization of the

dynamics of Cas3 in real time. Notably, experiments were performed in absence of Co^{2+} , unless explicitly stated in the text. To visualize the dynamics of Cas3, Cy3 molecules were excited an area of $50 \times 50 \mu\text{m}^2$ with a 28% of the full laser power (9 mW) green laser (532nm), while the time resolution was set to 0.1 s. Under these imaging conditions we obtained a high signal-to-noise ratio that allowed us to visualize kinetic intermediates while imaging over time periods of 3.5 min. Under these conditions photobleaching of the donor and acceptor dye during our observation time was minimized.

Single-molecule fluorescence data analysis

A series of CCD images were acquired with laboratory-made software at a time resolution of 0.1 s. Fluorescence time traces were extracted with an algorithm written in IDL (ITT Visual Information Solutions) that picked fluorescence spots above a threshold with a defined Gaussian profile. The extracted time traces were analyzed using custom written MATLAB (MathWorks) and python algorithms. FRET efficiency was defined as the ratio between the acceptor intensity and the sum of the acceptor and donor intensities. The crosstalk between the two detection channels was not corrected to minimize any artifact in using the step-finder algorithm.

For dwell-time ($\Delta\tau$) analysis, the start and end of each reeling event was determined (Figure 3A). The start of each event was marked by an abrupt decrease in the donor signal, whereas the end of each event was marked by an abrupt increase in the donor signal (Figures 2B and 2C). Selecting the start and end of each event yielded the duration of each event, which was plotted in a histogram. These dwell-time distributions were fitted with a gamma distribution using maximum-likelihood estimations, which yielded an estimation of the number of hidden steps (N) and the rate per step (k). To obtain the global change in the velocity of Cas3 the number of hidden steps (N) and the rate per step (k) were converted to the effective rate ($k^{\text{effective}}, 1/\Delta\tau$). The effective rate ($k^{\text{effective}}, 1/\Delta\tau$) was obtained by dividing the rate per step (k) by the number of steps (N). Next, this effective rate was converted to velocity (bp/ s) by multiplying the effective rate by the FRET range of 22 base pairs (Figures S5A and S5B). The 95% confidence intervals (errors) of the dwell-times were obtained by empirical bootstrap analysis (Dekking, 2005).

The step-size was characterized by adopting an automated step-finder algorithm, described previously by (Kerssemakers et al., 2006) (L.L., J. Kerssemakers, C.J., C. Dekker, unpublished data). The step-finder algorithm yielded the average FRET value for each plateau, the size of each step in between the plateaus and the duration/ dwell-time ($\Delta\tau$) of each plateau. To be able to correlate the size of each step in FRET to distance in base pairs, a set of constructs was generated where the distance between donor and acceptor was systematically increased (Figures S5A and S5B). The slope of this calibration curve yielded a conversion factor, in which a change of $\Delta E = 0.05$ corresponds to a distance of one base pair. This allowed direct conversion of the step-size in FRET to distance in base pairs.

The dwell-time distributions for each step were fitted with a gamma distribution using maximum-likelihood estimations (MLE), which yielded an estimation of the number of hidden steps (N) and the rate per step (k). During MLE, each data point is weighted with equal importance. As a consequence, the minor populations in the tail of the distribution are given a substantial amount of priority during minimization of the fit. This causes the fit to widen, which results in an under-estimation of the number of steps and thereby an over-estimation of the rate per step. To correctly interpret data, only the data in the peak of the distribution was fitted, through the use a threshold (Figures S5G and S5H). Notably, the minor populations in the tail of the distribution may represent stalled helicases or enzymes that have a significantly slower velocity due to static disorder (Park et al., 2010).

QUANTIFICATION AND STATISTICAL ANALYSIS

Histograms and fits were generated using OriginPro (OriginLab). The averages and errors representing the number of cycles/ molecule (Figures 2D, 2E, and S2H), the number of productive binding events (Figure 2G), the unwinding distance (Figures 3D and 3E), DNA ruler (Figure S5B) and bulk degradation (Figures S1F and S1G), encompass a minimum of three replicates (n). The errors represent the standard error of the mean (SEM), which was defined as: $SEM = \sigma / \sqrt{n}$.

The averages and errors displayed in Figures S11, S21, S4A, S4B, S4C, 3B, 4E, 4F, and S5G were obtained through bootstrap analysis. In brief, for bootstrap analysis, 10^4 datasets were generated by random sampling with replacement from the original dataset. Each of these datasets were fitted with the respective fit (indicated in the figure legend) and then used to calculate the average and 95% confidence intervals, which was defined as: $CI(.95) = 1.96 * \sigma$.

Molecular Cell, Volume 70

Supplemental Information

**Repetitive DNA Reeling by the Cascade-Cas3
Complex in Nucleotide Unwinding Steps**

Luuk Loeff, Stan J.J. Brouns, and Chirlmin Joo

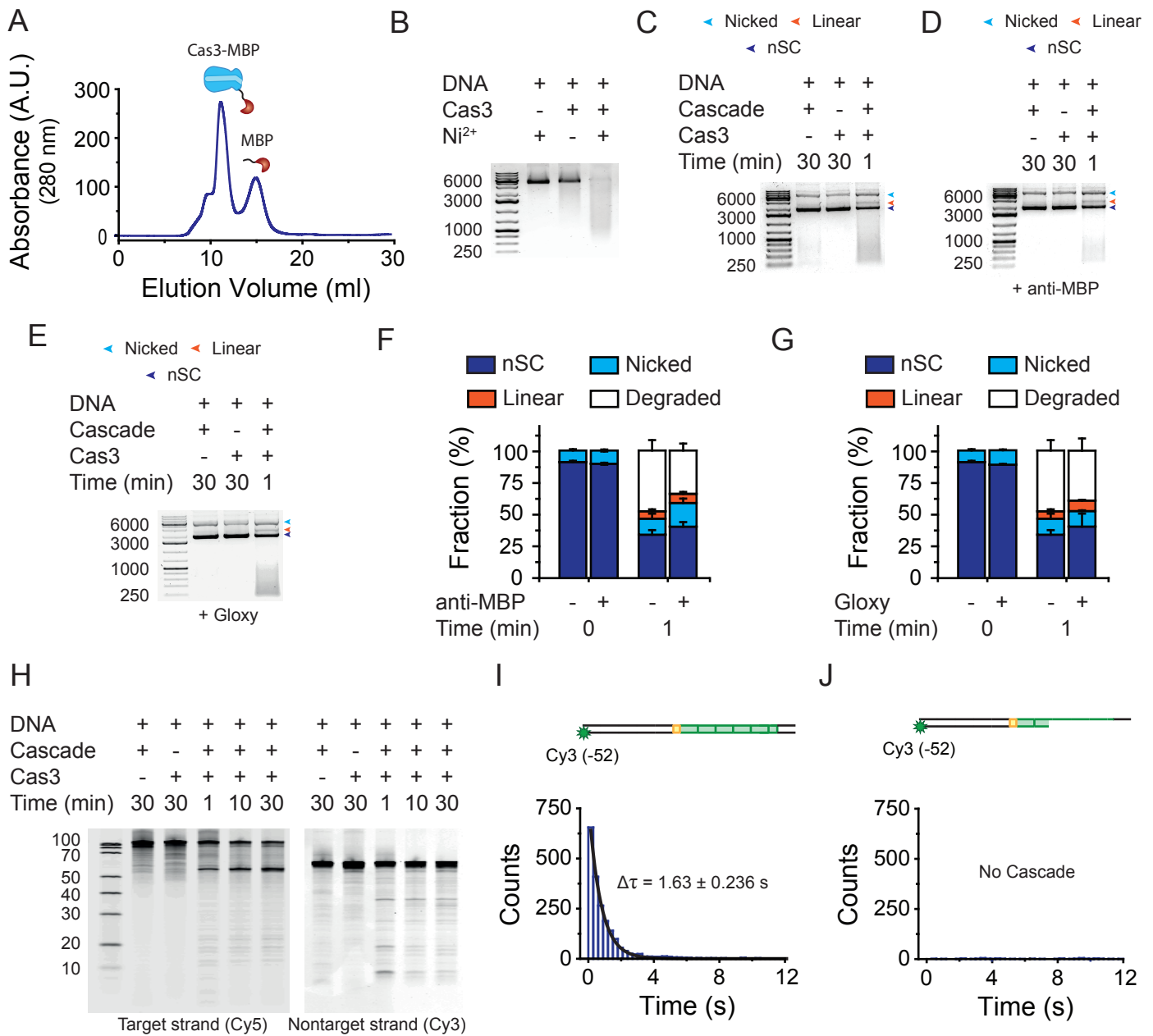


Figure S1. Purification and control experiments for Cas3 nuclease activity in bulk, related to Figure 1

(A) Gel filtration chromatogram of affinity purified Cas3-MBP. The two peaks correspond to Cas3-MBP and MBP. **(B)** Cas3 nuclease activity assay on single-stranded M13mp18 DNA. **(C)** Cas3 plasmid degradation assay. Negatively super-coiled (nSC), Nicked and linear DNA are indicated with the purple, cyan and orange arrows, respectively. **(D)** Cas3 plasmid degradation assay in presence of 600 nM anti-MBP antibody. Negatively super-coiled (nSC), Nicked and linear DNA are indicated with the purple, cyan and orange arrows, respectively. **(E)** Cas3 plasmid degradation assay in presence of 1x oxygen scavenging system. Negatively super-coiled (nSC), Nicked and linear DNA are indicated with the purple, cyan and orange arrows, respectively. **(F)** Comparison of the plasmid degradation efficiency in absence and presence of 600 nM anti-MBP antibody. Negatively super-coiled (nSC), Nicked and linear DNA are indicated with the purple, cyan and cyan bars, respectively. **(G)** Comparison of the plasmid degradation efficiency in absence and presence of 1x oxygen scavenging system. Negatively super-coiled (nSC), Nicked and linear DNA are indicated with the purple, cyan and cyan bars, respectively. **(H)** Cas3 degradation assay on dye-labeled oligonucleotides. The partial duplexed oligonucleotides (also see Figure 2A) consist of a PAM, protospacer and two flanks of 50 nt and 15 nt. Cy5 was attached to position -7 of the target strand and Cy3 to position -52 of the nontarget strand. **(I)** Dwell-time distribution of the interaction between Cas3 and Cascade bound to a cognate target, in absence of ATP and Co²⁺. Black line indicates a single-exponential fit. Error represents the 95% confidence interval obtained by bootstrap analysis. **(J)** Dwell-time distribution of the interaction between Cas3 and a cognate target, in absence of Cascade.

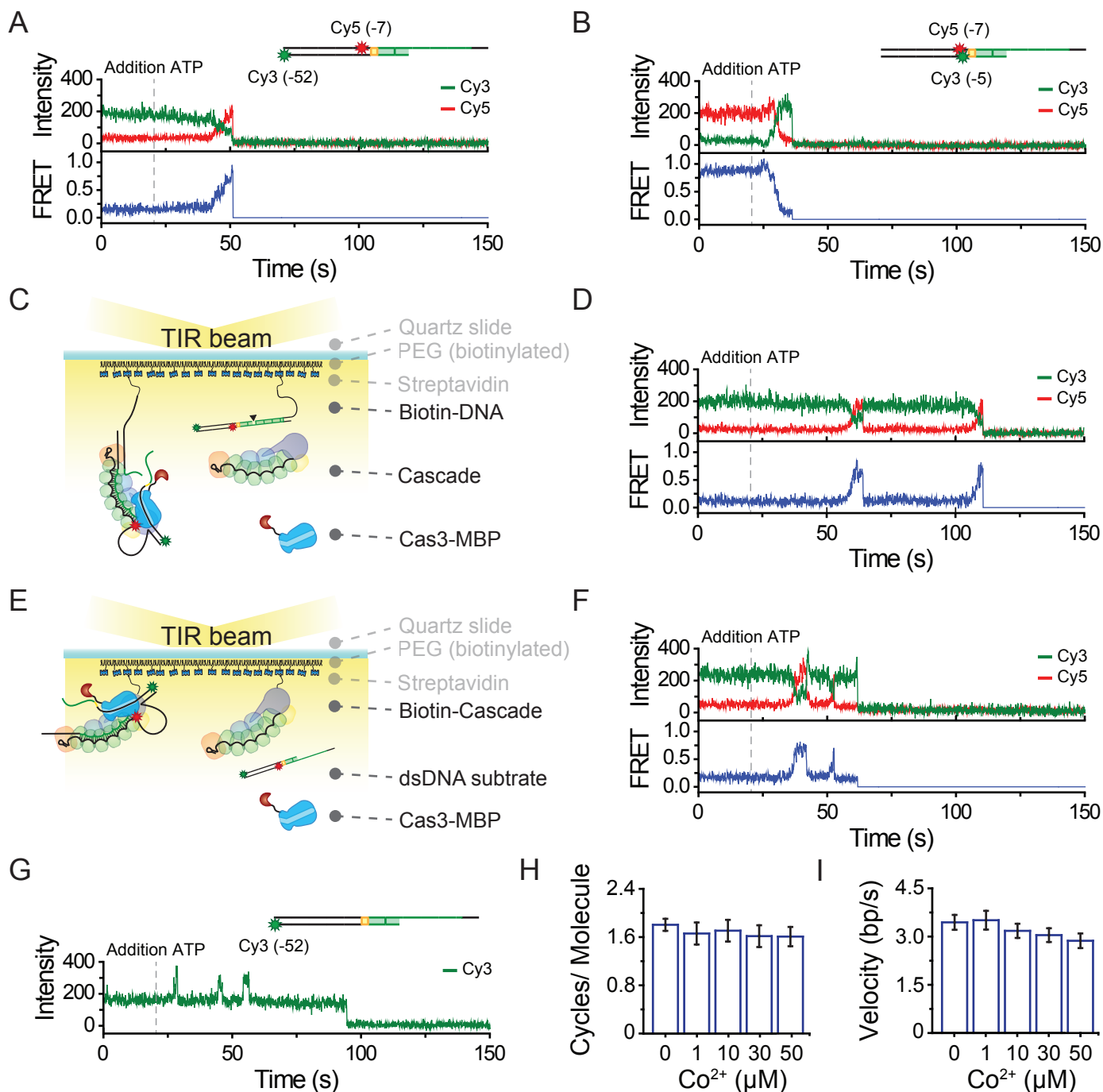


Figure S2. Representative traces and alternative immobilisation schemes, related to Figure 2

(A) A representative ATP time trace of donor (Cy3, green) and acceptor (Cy5, red) fluorescence and corresponding FRET (blue) exhibiting a single unwinding event. ATP (2 μ M) was added at t = 20s (dashed gray line). (B) A representative time trace for a construct with Cy5 (red star) attached to position -7 of the target strand and Cy3 (green star) to position -5 of the nontarget strand. ATP (2 μ M) was added at t = 20s (dashed gray line). (C) Schematic of an alternative single-molecule FRET assay used to probe reeling along the nontarget strand by Cas3. In brief, DNA was immobilized using biotin-streptavidin conjugation, followed by the addition of 10 nM Cascade. After incubation, Cas3 and ATP were introduced and the dynamics were followed in real-time. (D) A representative time trace for the immobilisation scheme depicted in [c]. ATP (2 μ M) together with Cas3 (10 nM) were added at t = 20s (dashed gray line). (E) Schematic of an alternative single-molecule FRET assay used to probe reeling along the non target strand by Cas3. In brief, biotinylated Cascade complexes were immobilized using biotin-streptavidin conjugation, followed by the addition of the DNA substrate. After incubation, Cas3 and ATP were introduced and the dynamics were followed in real-time. (F) A representative time trace for the immobilisation scheme depicted in [e]. ATP (2 μ M) together with Cas3 (10 nM) were added at t = 20s (dashed gray line). (G) A representative time trace of a construct labelled with a donor (Cy3, green) on the tracking strand, displaying PIFE. ATP (2 μ M) was added at t = 20s (dashed gray line). (H) Quantification of the number of unwinding cycles per molecule at various Co^{2+} concentrations. Error bars represent the SEM (N=3). (I) Quantification of the velocity at various Co^{2+} concentrations and 2 μ M ATP. Error bars represent 95% confidence intervals obtained through bootstrap analysis.

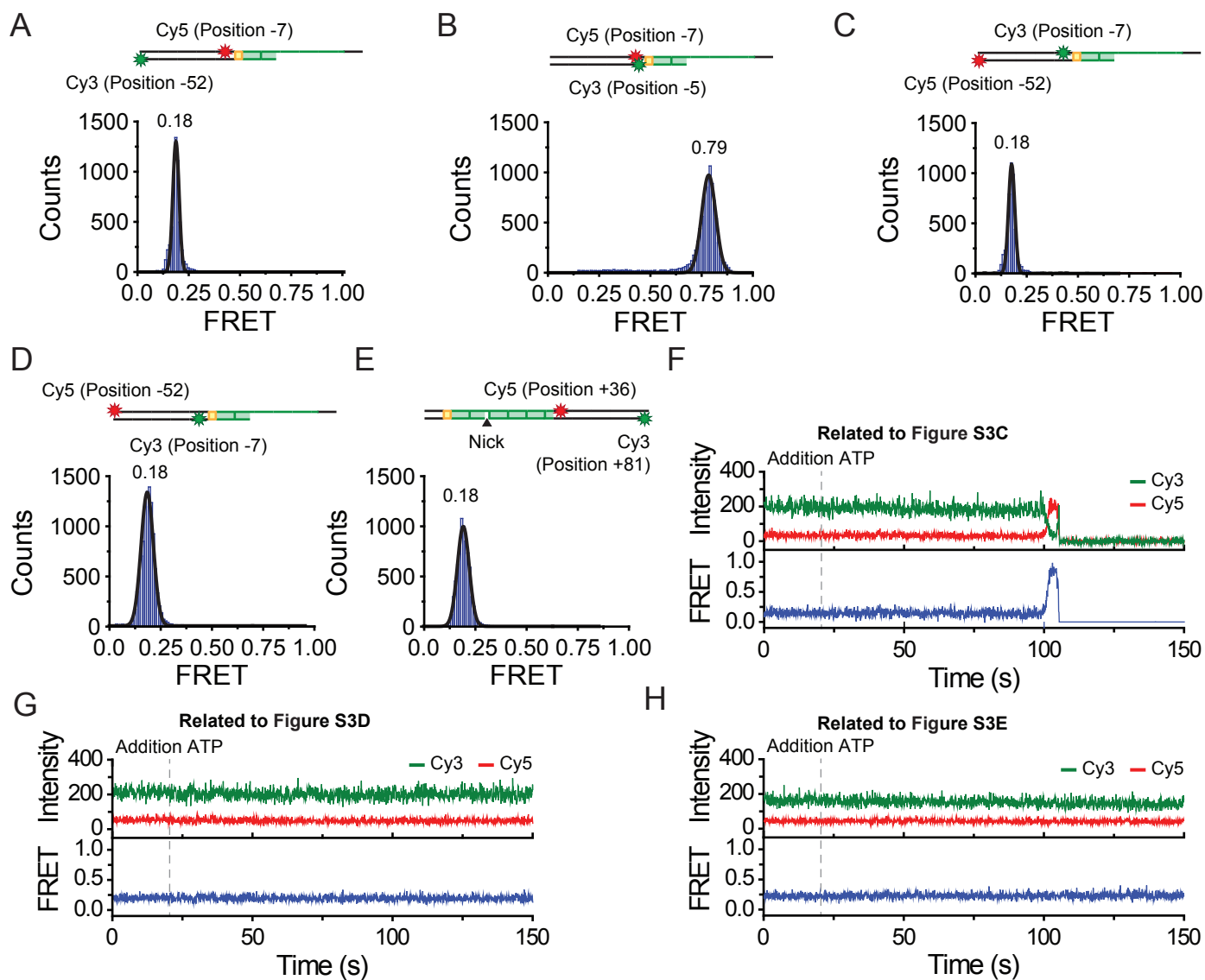


Figure S3. Initial FRET values and controls for reeling directionality by Cas3, related to Figure 2

(A) Initial FRET efficiency of a construct labelled at position -7 (Cy5, red star) of the target strand and at position -52 (Cy3, green star) of the nontarget strand. **(B)** Initial FRET efficiency of a construct labelled at position -7 (Cy5, red star) of the target strand and at position -5 (Cy3, green star) of the nontarget strand. **(C)** Initial FRET efficiency of a construct labelled at position -7 (Cy3, green star) of the target strand and at position -52 (Cy5, red star) of the nontarget strand. **(D)** Initial FRET efficiency of a construct labelled at position -52 (Cy5, red star) of the target strand and at position -7 (Cy3, green star) of the nontarget strand. **(E)** Initial FRET efficiency of a construct labelled at position +36 (Cy5, red star) of the target strand and at position +81 (Cy3, green star) of the nontarget strand. Black triangle indicates a nick at position +11. **(F)** A representative time trace for a construct labeled at position -7 (Cy3, green star) of the target strand and at position -52 (Cy5, red star) of the nontarget strand (see Figure S3C). ATP (2 μ M) was added at $t = 20$ s (dashed gray line). **(G)** A representative time trace for a construct labelled at position -52 (Cy5) of the target strand and at position -7 (Cy3) of the nontarget strand. (see Figure S3D). ATP (2 μ M) was added at $t = 20$ s (dashed gray line). **(H)** A representative time trace for a construct labelled at position +36 (Cy5) of the target strand and at position +81 (Cy3) of the nontarget strand (see Figure S3E). ATP (2 μ M) was added at $t = 20$ s (dashed gray line).

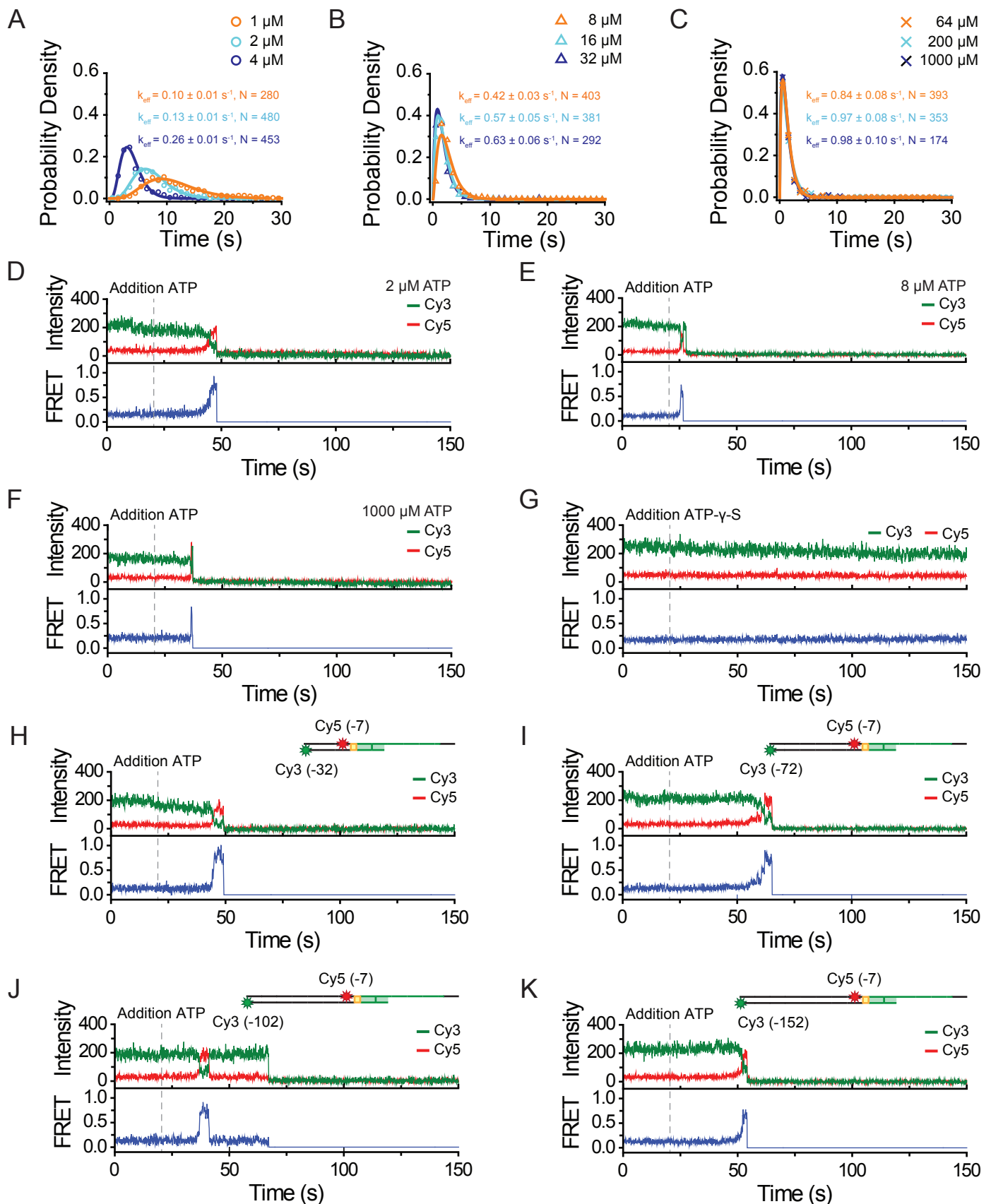


Figure S4. Dwell-time distributions and representative traces from ATP and length titration, related to Figure 3

(A-C) Dwell-time ($\Delta\tau$) distributions obtained by performing reeling assays at various ATP concentrations. Data is fitted with a gamma distribution (solid line) to obtain the effective rate ($k_{\text{eff}} = 1/\Delta\tau$). Error represents the 95% confidence interval obtained through bootstrap analysis. **(D-E)** Representative time traces of donor (Cy3, green) and acceptor (Cy5, red) fluorescence and corresponding FRET (blue) obtained at various ATP concentrations (2, 8, 1000 μM). **(G)** A representative time trace of donor (Cy3, green) and acceptor (Cy5, red) fluorescence and corresponding FRET (blue). ATP- γ -S (2 μM) was added at $t = 20\text{s}$ (dashed gray line). **(H-K)** Representative time trace of donor (Cy3, green) and acceptor (Cy5, red) fluorescence and corresponding FRET (blue) obtained from constructs with various flank lengths (30, 70, 100 and 150 bp). ATP was added at $t = 20\text{s}$ (dashed gray line).

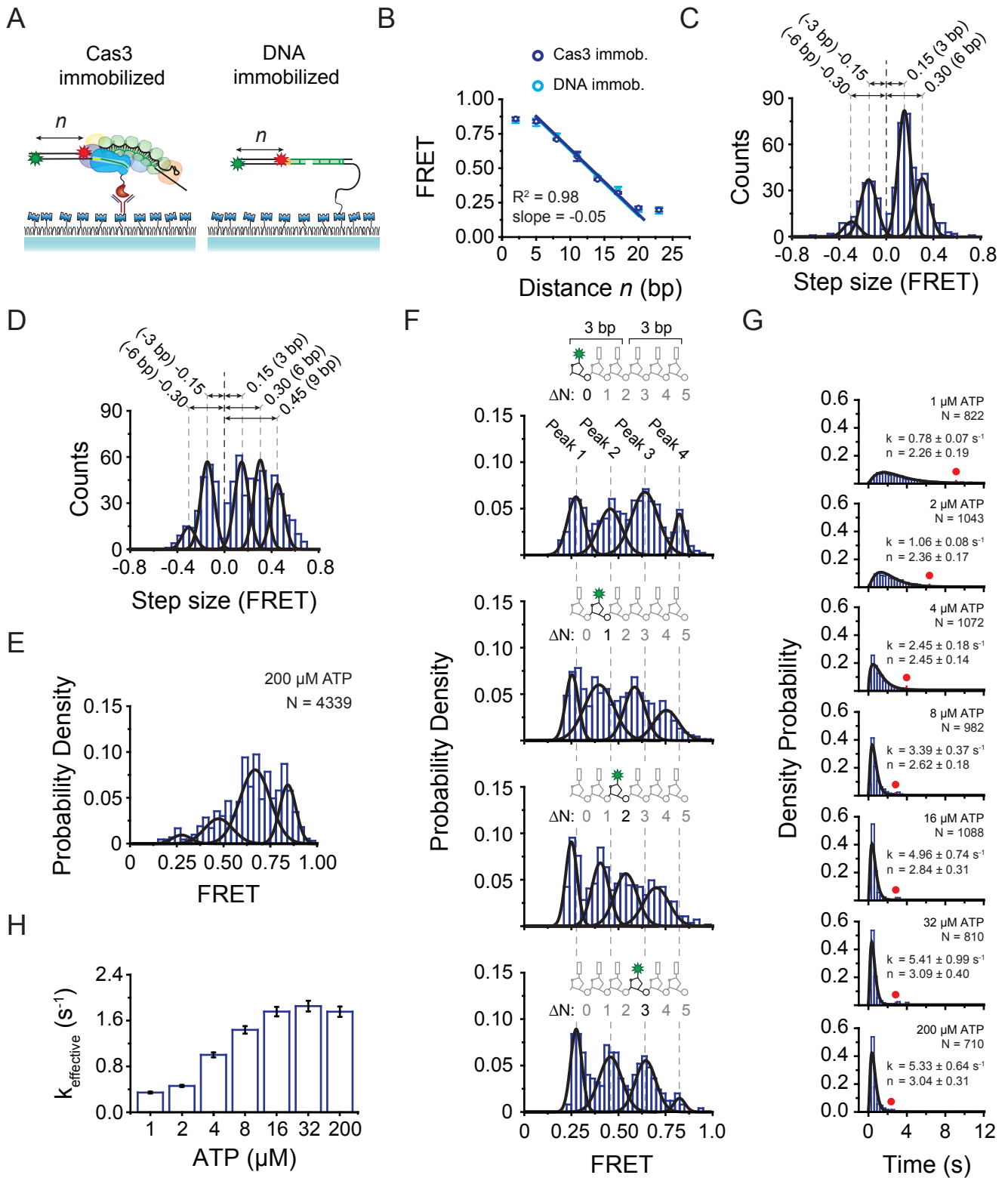


Figure S5. Calibration and distributions of the FRET levels and step-sizes obtained through a step-finder algorithm, related to Figure 4

(A) Schematic of the immobilization schemes used for the distance dependence measurement. **(B)** Distance dependence of FRET on double stranded DNA. For this control experiment, a series of DNA constructs were synthesized with different dye labelling positions. DNA was immobilized in either the presence of Cascade and Cas3 (purple circles) or through direct immobilization of the DNA (cyan circles). For both immobilization schemes, the FRET between donor and acceptor show a linear dependence on over a large FRET range. Error represents SEM of three individual measurements. **(C)** Distribution of step-sizes in FRET obtained in the presence of 10 μM ATP through the use of a step-finder algorithm. Black lines represent a Gaussian fit. Dashed grey lines indicate the centre of each peak. Positive values represent processive unwinding whereas negative values represent slipping. **(D)** Distribution of step-sizes in FRET obtained in the presence of 200 μM ATP through the use of a step-finder algorithm. Black lines represent a Gaussian fit. Dashed grey lines indicate the centre of each peak. Positive values represent processive unwinding whereas negative values represent slipping. **(E)** Distribution of FRET levels obtained in the presence of 200 μM ATP through the use of a step-finder algorithm. Black lines represent a Gaussian fit. **(F)** Distribution of the FRET levels for various positions of the donor dye. $\Delta N=0$ indicates the original dye position, whereas $\Delta N=1, 2$ or 3 indicates by how many nucleotides the donor dyes has moved from its original position. Markedly, peak 1 shows a less prominent shift compared to the other peaks (Figure 4D), whereas peak 4 broadens for the constructs with a donor dye at position $\Delta N=1$ & $\Delta N=2$. Given that these two peaks are located on the lower and upper boundary of the FRET range, the subtle changes in the peak position and shape reflect the detection limit of FRET. **(G)** Dwell-time ($\Delta\tau$) distributions per FRET level at various ATP concentrations. Data is fitted with a gamma distribution (black line) to obtain an estimate of the number of hidden steps (n) and the rate per step (k). The red dashed line indicates the threshold that was used to prevent fitting of the minor populations in the tail of the distribution. Error represents the 95% confidence interval obtained through bootstrap analysis. **(H)** The effective rate (K_{eff}) of individual plateaus at various ATP concentrations. Error represents the 95% confidence interval obtained through bootstrap analysis.

Table S1. List of used synthetic oligos for this study, related to Figure 1, 2, 3 & 4

Construct (label pos.)	Sequence ^a (5' → 3')	Description
TJ3_15_tar_30 (-7)	TAAGTAAGAGTAGGAGACAGCCCACATGGCATTCCACTTATCACTGGCATTAT/ iAmMC6T/GATCGTTCGTATTCTGCTGACGATAG	Substrate used for varying the length of flanking sequence
nTJ3_15_tar_30 (-32)	C/iAmMC6T/ATCGTCAGCAGAATACGAACGATCAATAATGCCAGTGATAAG	Substrate used for varying the length of flanking sequence
TJ3_15_tar_50 (-7)	TAAGTAAGAGTAGGAGACAGCCCACATGGCATTCCACTTATCACTGGCATTAT/ iAmMC6T/GATCGTTCGTATTCTGCTGACGATTGTAACGACAGTTCTGTTGAAT	Substrate to show loop formation
nTJ3_15_tar_50 (-52)	A/iAmMC6T/TCAACAGAACTGTCGTTACAATCGTCAGCAGAATACGAACGAT- CAATAATGCCAGTGATAAG	Substrate to show loop formation
nTJ3_15_tar_50 (-5)	ATTCAACAGAACTGTCGTTACAATCGTCAGCAGAATACGAACGATCAA/ iAmMC6T/AATGCCAGTGATAAG	Control substrate to verify loop formation
TJ3_15_tar_70 (-7)	TAAGTAAGAGTAGGAGACAGCCCACATGGCATTCCACTTATCACTGGCATTAT/ iAmMC6T/GATCGTTCGTATTCTGCTGACGGTCGTAACGACAGTTCTGTTGTTT- TATCACTGGTACAATCCAAC	Control substrate to verify loop formation
nTJ3_15_tar_70 (-72)	G/iAmMC6T/TGGATTGTACCAGTGATAATTCAACAGAACTGTCGTTACGACCGT- CAGCAGAATACGAACGATCAATAATGCCAGTGATAAG	Substrate used for varying the length of flanking sequence
TJ3_15_tar_100 (-7)	TAAGTAAGAGTAGGAGACAGCCCACATGGCATTCCACTTATCACTGGCATTAT/ iAmMC6T/GATCGTTCGTATTCTGCTGACGGTCGTAACGACAGTTCTGTTGTTT- TATCACTGGTACAATCCACTGCAACTGACACGATACTGTATCAATAATAG	Substrate used for varying the length of flanking sequence
nTJ3_15_tar_100 (-102)	C/iAmMC6T/ATTATTGATACAGTATCGTGTGTCAGTTGCAGTGATTGTAC- CAGTGATAATTCAACAGAACTGTCGTTACGACCGTCAGCAGAATACGAACGAT- CAATAATGCCAGTGATAAG	Substrate used for varying the length of flanking sequence
TJ3_15_tar_150 (-7)	TAAGTAAGAGTAGGAGACAGCCCACATGGCATTCCACTTATCACTGGCATTAT/ iAmMC6T/GATCGTTCGTATTCTGCTGACGGTCGTAACGACAGTTCTGTTGTTT- TATCACTGGTACAATCCACTGCAACTGACACGATACTGTATCAATAATAGGTT- CACCAACAGTCGATACTGAATGTCACACAGCACAGACAAATCACAAC	Substrate used for varying the length of flanking sequence
nTJ3_15_tar_150 (-152)	G/iAmMC6T/TGTGATTTGTCTGTGCTGTGTGACATTCAGTATCGACTGTTGGT- GAACCTATTATTGATACAGTATCGTGTGTCAGTTGCAGTGATTGTACCAGTGATAAT- TCAACAGAACTGTCGTTACGACCGTCAGCAGAATACGAACGATCAATAATGC- CAGTGATAAG	Substrate used for varying the length of flanking sequence
TJ3_15_tar_50 (-52)	TAAGTAAGAGTAGGAGACAGCCCACATGGCATTCCACTTATCACTGGCATTATA- GATCGTTCGTATTCTGCTGACGATTGTAACGACAGTTCTGTTGA/iAmMC6T/T	Control substrate to verify loop formation
nTJ3_15_tar_50 (-7)	AATCAACAGAACTGTCGTTACAATCGTCAGCAGAATACGAACGATC/iAmMC6T/ ATAATGCCAGTGATAAG	Control substrate to verify loop formation
TJ3_50_tar_15 (+36)	TAAGTTGTCTTGACAGCAATGTTAGCAGTCGTCTTATGCTTGCTAG/iAmMC6T/ TATGACAGCCCACATGGCATTCCACTTATCACTGGCATAGGATGAGAATGAAT	Control substrate to verify directionality of Cas3
nTJ3_50_tar_15 (+81) (I)	TGTGGGCTGTCATAACTAGCAAGTATAAGACGACTGCTAACATTGCTGTCAAGA- CAACT/iAmMC6T/A	Control substrate to verify directionality of Cas3
nTJ3_50_tar_15 (II)	ATTCATTCTCATCCTATGCCAGTGATAAGTGGAAATGCCA	Control substrate to verify directionality of Cas3

^a /iAmMC6T/ refers to an amino-modified thymine base at the indicated position.

Construct (label pos.)	Sequence ^a (5' → 3')	Description
TJ3_15_tar_30 (-7)	TAAGTAAGAGTAGGAGACAGCCCACATGGCATTCCACTTATCACTGGCATTAT/ iAmMC6T/GATCGTTCGTATTCTGCTGACGATAG	Substrate used for varying the length of flanking sequence
TJ3_15_tar_50 (-7)	TAAGTAAGAGTAGGAGACAGCCCACATGGCATTCCACTTATCACTGGCATTAT/ iAmMC6T/GATCGTTCGTATTCTGCTGACGATTGTAACGACAGTTCTGTGAATT	Control substrate to verify 3-bp periodicity
nTJ3_15_tar_50 (-51)	AA/iAmMC6T/TCACAGAAGTGTCTTACAATCGTCAGCAGAATACGAACGAT- CAATAATGCCAGTGATAAG	Control substrate to verify 3-bp periodicity
TJ3_15_tar_50 (-7)	TAAGTAAGAGTAGGAGACAGCCCACATGGCATTCCACTTATCACTGGCATTAT/ iAmMC6T/GATCGTTCGTATTCTGCTGACGATTGTAACGACAGTTCTGGAATTT	Control substrate to verify 3-bp periodicity
nTJ3_15_tar_50 (-50)	AAA/iAmMC6T/TCCAGAAGTGTCTTACAATCGTCAGCAGAATACGAACGAT- CAATAATGCCAGTGATAAG	Control substrate to verify 3-bp periodicity
TJ3_15_tar_50 (-7)	TAAGTAAGAGTAGGAGACAGCCCACATGGCATTCCACTTATCACTGGCATTAT/ iAmMC6T/GATCGTTCGTATTCTGCTGACGATTGTAACGACAGTTCTGAAGTTT	Control substrate to verify 3-bp periodicity
nTJ3_15_tar_50 (-49)	AAAC/iAmMC6T/TCAGAAGTGTCTTACAATCGTCAGCAGAATACGAACGAT- CAATAATGCCAGTGATAAG	Control substrate to verify 3-bp periodicity
TJ3_15_tar_33 (-7)	TAAGTAAGAGTAGGAGACAGCCCACATGGCATTCCACTTATCACTGGCATTAT/ iAmMC6T/TGAACGATCATAATCAGCAGCAGTATA	Control substrate for FRET based ruler
nTJ3_15_tar_33 (-10)	TATACTGCTGCTGATTATGATCG/iAmMC6T/TCAATAATGCCAGTGATAAG	Control substrate for FRET based ruler
nTJ3_15_tar_33 (-13)	TATACTGCTGCTGATTATGA/iAmMC6T/CGTTCAATAATGCCAGTGATAAG	Control substrate for FRET based ruler
nTJ3_15_tar_33 (-16)	TATACTGCTGCTGATTA/iAmMC6T/GATCGTTCAATAATGCCAGTGATAAG	Control substrate for FRET based ruler
nTJ3_15_tar_33 (-19)	TATACTGCTGCTGA/iAmMC6T/TATGATCGTTCAATAATGCCAGTGATAAG	Control substrate for FRET based ruler
nTJ3_15_tar_33 (-22)	TATACTGCTGC/iAmMC6T/GATTATGATCGTTCAATAATGCCAGTGATAAG	Control substrate for FRET based ruler
nTJ3_15_tar_33 (-25)	TATACTGC/iAmMC6T/GCTGATTATGATCGTTCAATAATGCCAGTGATAAG	Control substrate for FRET based ruler
nTJ3_15_tar_33 (-28)	TATAC/iAmMC6T/GCTGCTGATTATGATCGTTCAATAATGCCAGTGATAAG	Control substrate for FRET based ruler
nTJ3_15_tar_33 (-31)	TA/iAmMC6T/ACTGCTGCTGATTATGATCGTTCAATAATGCCAGTGATAAG	Control substrate for FRET based ruler
Biotin_linker	AAAATTGAGCAGACCAAA(PolyT) ₆₂ - Biotin	Biotin linker used for immobilisation

^a /iAmMC6T/ refers to an amino-modified thymine base at the indicated position.